Mon. Not. R. Astron. Soc. **000**, 000–000 (0000) Printed 18 June 2008 (MN LATEX style file v2.2)

Stellar Populations of Bulges in 14 Cluster Disc Galaxies⋆

L. Morelli[1,5], E. Pompei[2], A. Pizzella[1], J. Méndez-Abreu[1,3], E. M. Corsini[1], L. Coccato[4], R. P. Saglia[4], M. Sarzi[6] and F. Bertola[1]

[1] *Dipartimento di Astronomia, Università di Padova, vicolo dell'Osservatorio 3, I-35122 Padova, Italy.*
[2] *European Southern Observatory, 3107 Alonso de Cordova, Santiago, Chile.*
[3] *INAF-Osservatorio Astronomico di Padova, vicolo dell'Osservatorio 5, I-35122 Padova, Italy.*
[4] *Max-Planck Institut für extraterrestrische Physik, Giessenbachstrasse, D-85748 Garching, Germany.*
[5] *Department of Astronomy, Católica de Chile, Pontificia Universidad, Vicuna Mackenna 4860, Casilla 306, Santiago 22, Chile*
[6] *Centre for Astrophysics Research, University of Hertfordshire, College Lane, Hatfield, Herts AL10 9AB*

Accepted 2008 June 11. Received 2008 May 13; in original form 2008 January 15

ABSTRACT

Photometry and long-slit spectroscopy are presented for 14 S0 and spiral galaxies of the Fornax, Eridanus and Pegasus cluster, and NGC 7582 group. The structural parameters of the galaxies are derived from the $R-$band images by performing a two-dimensional photometric decomposition of the surface-brightness distribution. This is assumed to be the sum of the contribution of a bulge and disc component characterized by elliptical and concentric isophotes with constant (but possibly different) ellipticity and position angles. The rotation curves and velocity dispersion profiles are measured from the spectra obtained along the major axis of galaxies. The radial profiles of the H_β, Mg, and Fe line-strength indices are presented too. Correlations between the central values of Mg_2, $\langle\mathrm{Fe}\rangle$, H_β, and σ are found. The age, metallicity and α/Fe enhancement of the stellar population in the center and at the radius where bulge and disc give the same contribution to the total surface brightness are obtained using stellar population models with variable element abundance ratios. Three classes of bulges are identified. The youngest bulges (~ 2 Gyr) with ongoing star formation, intermediate-age bulges (4–8 Gyr) have solar metallicity, and old bulges (~ 10 Gyr) have high metallicity. Most of the sample bulges display solar α/Fe enhancement, no gradient in age, and a negative gradient of metallicity. The presence of negative gradient in the metallicity radial profile favors a scenario with bulge formation via dissipative collapse. This implies strong inside-out formation that should give rise to a negative gradient in the α/Fe enhancement too. But, no gradient is measured in the $[\alpha/\mathrm{Fe}]$ radial profiles for all the galaxies, except for NGC 1366. In this galaxy there is a kinematically-decoupled component, which is younger than the rest of host bulge. It possibly formed by enriched material probably acquired via interaction or minor merging. The bulge of NGC 1292 is the most reliable pseudobulge of our sample. The properties of its stellar population are consistent with a slow buildup within a scenario of secular evolution.

Key words: galaxies : abundances – galaxies : bulges – galaxies : evolution – galaxies : stellar content – galaxies : formation – galaxies : Kinematics and Dynamics

1 INTRODUCTION

The relative importance of the dissipative collapse (Eggen et al. 1962; Sandage 1990; Gilmore & Wyse 1998), major and minor merging events (Kauffmann 1996; Cole et al. 2000; Aguerri et al. 2001), and redistribution of disc material due to the presence of a bar or environmental effects (Kormendy & Kennicutt 2004) drives the variety of properties observed in bulges.

The bulges of lenticulars and early-type spirals are similar to low-luminosity elliptical galaxies. Their photometric and kinematic properties satisfy the same fundamental plane correlation (FP) found for ellipticals (Bender et al. 1992, 1993; Burstein et al. 1997; Aguerri et al. 2005). The surface-brightness radial profile of big bulges is well described by the de Vaucouleurs law (Andredakis et al. 1995; Carollo et al. 1998; Möllenhoff & Heidt 2001) **even if this could drastically change by taking into ac-**

⋆ Based on observations made with ESO Telescopes at the La Silla observatory under programmes 70.B-0486 and 71.B-0202.

count the small-scale inner structures smoothed by the seeing in the ground-base observations (Balcells et al. 2003). Some of them are rotationally-flattened oblate spheroids with little or no anisotropy (Kormendy & Illingworth 1982; Davies & Illingworth 1983; Cappellari et al. 2006). But, the intrinsic shape of a large fraction of early-type bulges is triaxial, as shown by the isophotal twisting (Lindblad 1956; Zaritsky & Lo 1986), misalignment with respect to disc (Bertola et al. 1991; Mendez-Abreu et al. 2007), and non-circular gas motions (Bertola et al. 1989; Gerhard et al. 1989; Berman 2001; Corsini et al. 2003; Coccato et al. 2004). The bulk of their stellar population formed between redshift 3 and 5 ($\simeq$12 Gyr) in a short time-scale (Bernardi et al. 1998; Mehlert et al. 2003; Thomas et al. 2005). The enrichment of interstellar medium is strongly related to the time delay between SNII and SNIa, which contributed most of the α elements and Iron, respectively (Worthey et al. 1992; Thomas et al. 2003).

On the contrary, the bulges of late-type spiral galaxies are reminiscent of discs. They are flat components (Fathi & Peletier 2003) with exponential surface-brightness radial profiles (Andredakis & Sanders 1994; de Jong 1996; MacArthur et al. 2003) and rotate as fast as discs (Kormendy 1993; Kormendy et al. 2001). Moreover, the stellar population in late-type bulges is younger than in early-type bulges (Trager et al. 1999; Goudfrooij et al. 1999; Thomas & Davies 2006). They appear to have lower metallicity (Ganda et al. 2007) and lower α/Fe enhancement with respect to early type galaxies (Proctor & Sansom 2002; Peletier et al. 2007; Afanasiev & Sil'chenko 2005).

In the current paradigm, early-type bulges were formed by rapid collapse and merging events while late-type bulges have been slowly assembled by internal and environmental secular processes (Kormendy & Kennicutt 2004). But many questions are still open. For instance, the monolithic collapse can not explain the presence in bulges of kinematically-decoupled components (Pizzella et al. 2002; Krajnović & Jaffe 2004; Emsellem et al. 2004; McDermid et al. 2006). Moreover, the environment plays a role in defining the properties of galaxies (e.g., Dressler 1980; Coziol et al. 2001; Clemens et al. 2006; Brough et al. 2007). Recent studies of early-type galaxies in different environments (Beuing et al. 2002; Thomas et al. 2005; Thomas & Davies 2006) have shown that age, metallicity, and α/Fe enhancement are more correlated with the total mass of the galaxy than local environment.

To investigate the formation and evolution of the bulges, there are two possible approaches: going backward in redshift and look to evolution of galaxies through cosmic times or analyze in detail nearby galaxies to understand the properties of their stellar population in terms of dominant mechanism at the epochs of star formation and mass assembly. In this work, we present a photometric and spectroscopic study of the bulge dominated region of a sample of spiral galaxies in the Fornax and Pegasus clusters. Our aim is to estimate the age and metallicity of the stellar population and the efficiency and timescale of the last episode of star formation to disentangle between early rapid assembly and late slow growing.

The galaxy sample is presented in Sect. 2. The photometric observations are described in Sect. 3.1. The structural parameters of the bulge and disc of the sample galaxies are derived by analyzing their two-dimensional surface brightness distribution in Sect. 3.2. The spectroscopic observations are described in Sect. 4.1. The stellar kinematics and line-strength indices are measured from long-slit spectra in Sect. 4.2. The central values of the line-strength indices are derived in Sect. 5. They are used to estimate the age, metallicity, and α/Fe-enhancement of the stellar population of the bulge in Sect. 6 . Their gradients in the bulge dominated region are discussed in Sect. 7. The identification of pseudobulges hosted by sample galaxies is performed in Sect. 8. Finally, conclusions are given in Sect. 9.

2 SAMPLE SELECTION

The main goal of this paper is to study the stellar populations in bulges. In order to simplify the interpretation of the results we selected a sample of disc galaxies, which do not show any morphological signature of having undergone a recent interaction event. All the observed galaxies are classified as unbarred or weakly barred galaxies by de Vaucouleurs et al. (1991, hereafter RC3). They are bright ($B_T \leqslant 13.5$, RC3) and nearby ($V_{\rm CMB} < 4500$ km s^{-1}, RC3) lenticulars and spirals with a low-to-intermediate inclination ($i \leqslant 65^\circ$, RC3). 12 of them were identified as member of either the Fornax, Eridanus and Pegasus cluster and 2 are member of the NGC 7582 group (Ferguson 1989; Fouque et al. 1992; Garcia 1993; Nishiura et al. 2000). The final sample is formed by 12 disc cluster and 2 group galaxies.

For every galaxy we provide the local galaxy number density using the method of distance to the $5^{\rm th}$ nearest neighbour (Balogh et al. 2004). The projected galaxy density can be defined by $\Sigma_5 = 5/(\pi d_5^2)$, where d_5 is the distance to the 5^{th} nearest neighbour. To this aim we adopted the catalog of galaxies available in the Hyperleda database (Paturel et al. 2003). We considered only galaxies brighter than $M_B > -16$ with systemic velocity in a range between ± 1000 km s^{-1} with respect to the velocity of the sample galaxy (to avoid the background/foreground contamination). The sample galaxies reside in a high-density environment. In fact, their Σ_5 is much higher than the typical value of the field galaxies ($\Sigma_5 = 0.05$ Balogh et al. 2004).

The galaxy number density along with an overview of the basic properties of the sample galaxies is given in Table 1.

3 SURFACE PHOTOMETRY

3.1 Observations and data reduction

The photometric observations of the sample galaxies were carried out in two runs at the European Southern Observatory (ESO) in La Silla (Chile) on December 2002, 9-12 (run 1), September 2003, 26-28 (run 2).

We imaged the galaxies at the ESO 3.6-m Telescope with the ESO Faint Object Spectrograph and Camera 2 (EFOSC2). The detector was the No. 40 Loral/Lesser CCD with 2048×2048 pixels of 15×15 μm^2. A 2×2 pixel binning was adopted giving an effective scale of 0.314 arcsec pixel^{-1} with a field of view of 5.3×8.6 arcmin^2. The gain and readout noise were set to 1.3 e$^-$ ADU^{-1} and 9 e$^-$, respectively.

We used the No. 642 Bessel R-band filter centred at 6431 Å with a FWHM of 1654 Å. For each galaxy we took $2 \times 60-$s images with a offset of few pixels to be able to clean cosmic rays and bad pixels. Every night we observed several fields of standard stars at different air-masses to be used for the flux calibration. For each field we took different exposures ranging from 5 to 15 s to have good signal-to-noise ratio (S/N) and well sampled PSF for all the standard stars. The typical value of the seeing FWHM during the galaxy exposures was 1.0 arcsec as measured by fitting a two-dimensional Gaussian to the field stars.

Table 1. Properties of the sample galaxies. The columns show the following: (2) the morphological classification from RC3; (3) numerical morphological type from RC3. The values marked with * were derived from the galaxy B/T ratio following the morphology-B/T relation by Graham (2001); (4) major-axis position angle adopted for spectroscopic observations; (5) apparent isophotal diameters measured at a surface-brightness level of $\mu_B = 25$ mag arcsec^{-2} from RC3; (6) total observed blue magnitude from RC3, except for ESO 358-50 from Lyon Extragalactic Database (LEDA); (7) radial velocity with respect to the CMB radiation from RC3; (8) distance obtained as luminosity-weighted mean radial velocity (Garcia 1993) divided by $H_0 = 75$ km s^{-1} Mpc^{-1}; (9) absolute total blue magnitude from B_T corrected for inclination and extinction as in LEDA and adopting D; (10) membership to Fornax (F) Eridanus (E) Pegasus (P) cluster or NGC 7582 group according to (Ferguson 1989; Fouque et al. 1992; Garcia 1993; Nishiura et al. 2000); (11) projected galaxy density defined as in Balogh et al. (2004)

Galaxy	Type	T	PA	$D_{25} \times d_{25}$	B_T	$V_{\rm CMB}$	D	$M^0_{B_T}$	Cluster	Density
	(RC3)	(RC3)	(°)	(arcmin)	(mag)	(km s^{-1})	(Mpc)	(mag)		Σ_5
(1)	(2)	(3)	(4)	(5)	(6)	(7)	(8)	(9)	(10)	(11)
ESO 358-50	SA0^0?	-2.0	173	1.7×0.7	13.87	1154	17.0	-17.34	F	11.0
ESO 548-44	SA(r)0$^+$:	-1.5	60	1.2×0.5	14.53	1561	22.6	-17.66	E	19.3
IC 1993	(R$'$)SAB(rs)b	3.0	57	2.5×2.1	12.43	877	17.0	-18.81	F	6.2
IC 5267	SA(s)0/a	0.0	140	5.2×3.9	11.43	1480	21.5	-20.38	N 7582	2.2
IC 5309	Sb	3.0	23	1.3×0.6	14.52	3840	50.2	-19.64	P	7.6
NGC 1292	SAb(s)	5.0	7	3.0×1.3	11.29	1227	17.0	-18.90	F	4.0
NGC 1351	SA$^-$pec:	-3.0	140	2.8×1.7	12.46	1407	17.0	-18.67	F	31.3
NGC 1366	S0^0	-2.0	2	2.1×0.9	11.97	1182	17.0	-18.30	F	10.1
NGC 1425	SA(s)b	3.0	129	5.8×2.6	11.29	1402	17.0	-20.25	F	2.1
NGC 7515	S?	3.0*	15	1.7×1.6	13.16	4117	50.2	-20.44	P	2.1
NGC 7531	SAB(r)bc	4.0	15	4.5×1.8	12.04	1361	21.5	-19.25	N 7582	4.8
NGC 7557	S?	4.0*	163	0.6×0.6	15.15	3366	50.2	-18.74	P	2.4
NGC 7631	SA(r)b:	3.0	79	1.8×0.7	13.93	3396	50.2	-20.38	P	19.1
NGC 7643	S?	6.0*	45	1.4×0.7	14.12	3520	50.2	-19.88	P	1.2

All images were reduced using standard IRAF[1] tasks. We first subtracted a bias frame consisting of ten exposures for each night. The images were flat-fielded using sky flats taken at the beginning and/or end of each observing night. The sky background level was removed by fitting a Legendre polynomial (with a degree free to range between 0 and 2) to the regions free of sources in the images. Special care was taken during sky subtraction to reach the outermost parts of the objects. No scattered light was observed in the images, and the adopted polynomial degree was either 0 or 1. Cosmic rays and bad pixels were removed by combining the different exposures using field stars as a reference and adopting a sigma clipping rejection algorithm. Residual cosmic rays and bad pixels were corrected by manually editing the combined image.

The photometric calibration constant includes only the correction for atmospheric extinction, which is taken from the differential aerosol extinction for ESO (Burki et al. 1995). No color term has been considered and no attempt was made to correct for internal and Galactic extinction. Fig. 1 shows the calibrated R-band images of the sample galaxies.

Isophote-fitting with ellipses, after masking foreground stars and residual bad columns, was carried out using the IRAF task ELLIPSE. In all cases, we first fit ellipses allowing their centres to vary. Within the errors, no variation in the ellipse centres was found for all the galaxies studied in this paper. The final ellipse fits were done at fixed ellipse centres. The ellipse-averaged profiles of surface brightness, position angle and ellipticity are shown in Fig. 1 for all the sample galaxies.

[1] IRAF is distributed by NOAO, which is operated by AURA Inc., under contract with the National Science Foundation.

3.2 Photometric decomposition

Let (x, y, z) be Cartesian coordinates with the origin corresponding to the position of the galaxy surface-brightness peak, the $x-$axis parallel to direction of right ascension and pointing westward, the $y-$axis parallel to direction of declination and pointing northward, and the $z-$axis along the line-of-sight and pointing toward the observer. The plane of the sky is confined to the (x, y) plane.

We assumed the galaxy surface-brightness distribution to be the sum of the contributions of a bulge and a disc component. Bulge isophotes are ellipses centred on (x_0, y_0), with constant position angle $\mathrm{PA_b}$ and constant axial ratio q_b. Disc isophotes are ellipses centred on (x_0, y_0), with constant position angle $\mathrm{PA_d}$ and constant axial ratio q_d, implying that the galaxy inclination is $i = \arccos q_\mathrm{d}$. We adopted the Sérsic law (Sersic 1968) to describe the surface brightness of the bulge component

$$I_\mathrm{b}(x, y) = I_\mathrm{e} 10^{-b_n\left[(r_\mathrm{b}/r_\mathrm{e})^{1/n}-1\right]}, \quad (1)$$

where r_e, I_e and n are respectively the effective radius, surface brightness at r_e, and a shape parameter describing the curvature of the profile. The value of b_n is coupled to n so that half of the total flux is always within r_e and can be approximated as $b_n = 0.868n - 0.142$ (Caon et al. 1993). The radius r_b is given by

$$\begin{aligned} r_\mathrm{b} \quad = \quad & \big[(-(x-x_0)\sin\mathrm{PA_b} + (y-y_0)\cos\mathrm{PA_b})^2 + \\ & (-(x-x_0)\cos\mathrm{PA_b} - (y-y_0)\sin\mathrm{PA_b})^2/q_\mathrm{b}^2\big]^{1/2} \end{aligned} \quad (2)$$

For the surface brightness distribution of the disc component we assumed the exponential law (Freeman 1970)

$$I_\mathrm{d}(x, y) = I_0\, e^{-r_\mathrm{d}/h}, \quad (3)$$

where h and I_0 are the scale length and central surface brightness

of the disc, respectively. The radius $r_{\rm d}$ is given by

$$r_{\rm d} = \left[(-(x-x_0)\sin{\rm PA_d}+(y-y_0)\cos{\rm PA_d})^2+ (-(x-x_0)\cos{\rm PA_d}-(y-y_0)\sin{\rm PA_d})^2/q_{\rm d}^2\right]^{1/2} \quad (4)$$

To derive the photometric parameters of the bulge ($I_{\rm e}$, $r_{\rm e}$, n, PA$_{\rm b}$, and $q_{\rm b}$) and disc (I_0, h, PA$_{\rm d}$, and $q_{\rm d}$) and the position of the galaxy centre (x_0, y_0) we fitted iteratively a model of the surface brightness $I_{\rm m}(x,y) = I_{\rm b}(x,y) + I_{\rm d}(x,y)$ to the pixels of the galaxy image using a non-linear least-squares minimization based on the robust Levenberg-Marquardt method by Moré et al. (1980). We adopted the technique for photometric decomposition developed in GASP2D by Mendez-Abreu et al. (2007). The actual computation has been done using the `MPFIT`[2] algorithm implemented by C. B. Markwardt under the `IDL`[3] environment. Each image pixel has been weighted according to the variance of its total observed photon counts due to the contribution of both the galaxy and sky, and determined assuming photon noise limitation and taking into account for the detector read-out noise. The seeing effects were taken into account by convolving the model image with a circular Gaussian PSF with the FWHM measured from the stars in the galaxy image. The convolution was performed as a product in Fourier domain before the least-squares minimization.

To derive the free parameters of the model surface-brightness distribution, we adopted as initial trial for least-squares minimization the values obtained by performing a standard photometric decomposition with a parametric technique similar to that adopted by Kormendy (1977). The ellipse-averaged surface-brightness profile of the galaxy has been fitted in two steps by considering first separately and then simultaneously the light contributions of the bulge and disc.

We began by fitting an exponential law to the galaxy surface-brightness profile at large radii, where it is dominated by the light contribution of the disc. In this way we derived the values of I_0 and h. Then we extrapolated the exponential profile to small radii and subtracted it from the galaxy surface-brightness profile. This gave us a first estimate of the light distribution of the bulge. We fitted to this a Sersíc profile by assuming the bulge shape parameter to be $n = 0.5, 1, 1.5, \ldots, 6$ and deriving the corresponding values of $I_{\rm e}$ and $r_{\rm e}$. Finally, for each set of $I_{\rm e}$, $r_{\rm e}$, n, I_0, and h we fitted simultaneously both bulge and disc to the galaxy surface-brightness profile and we assumed those giving the best fit as the trial values for the two-dimensional fit, where all the parameters are allowed to vary.

The trial values of PA$_{\rm b}$ and $q_{\rm b}$ were obtained by interpolating at $r_{\rm e}$ the ellipse-averaged position-angle and ellipticity profiles, respectively. We assumed the coordinates of the image pixel where the maximum galaxy surface brightness is measured as the trial values of the coordinates (x_0, y_0) of the galaxy centre. The parameters derived for the structural components of the sample galaxies are collected in Table 2. The result of the photometric decomposition of the surface brightness distribution of the sample galaxies is shown in Fig. 1.

The errors given in Table 2 were obtained through a series of Monte Carlo simulations. Due to the formal errors obtained from the χ^2 minimization method are usually not representative of the real errors in the structural parameters. We have carried out extensive simulations on artificial galaxies in order to give a reliable estimation of these errors.

We generated a set of 2000 images of galaxies with a Sérsic bulge and an exponential disc. The structural parameters of the artificial galaxies were randomly chosen among the following ranges

$$0.5 \leqslant r_e \leqslant 3\ {\rm kpc} \qquad 0.5 \leqslant {\rm q_b} \leqslant 0.9 \qquad 0.5 \leqslant {\rm n} \leqslant 6 \quad (5)$$

for the bulges, and

$$1 \leqslant h \leqslant 6\ {\rm kpc} \qquad 0.5 \leqslant {\rm q_b} \leqslant 0.9 \quad (6)$$

for the discs. The artificial galaxies also satisfy the following conditions

$$q_d \leqslant q_b \qquad 10 \leqslant m_R \leqslant 14\ {\rm mag} \quad (7)$$

where m_R is the total R-band magnitude of the galaxy. The simulated galaxies were assumed to be at a distance of ~ 29 Mpc, which correspond to a scale of ~ 141 pc arcsec^{-1}. The pixel scale used was 0.314 arcsec pixel^{-1} and the CCD gain and RON were 0.7 e$^-$ ADU^{-1} and 8 e$^-$ to mimic the instrumental setup of the observed galaxies. Finally, a background level and a photon noise were added to the resulting images to yield a signal-to-noise ratio similar to that of the observed images.

To estimate the errors associated to the decomposition, the code GASP 2D was applied to the artificial images as if they were real. Then, the relative errors (1- v$_i$/v$_o$) were estimated by comparing the input (v$_i$) and output (v$_o$) values. To assign to every single galaxy the corresponding error for every structural parameter, we divided our catalogue of artificial galaxies in bins of 0.5 magnitudes, we assumed that the errors were normally distributed, with mean and standard deviation corresponding to the systematic and typical error respectively. Then we placed our observed galaxy in its magnitude bin and assigned to every parameter the corresponding error.

4 LONG-SLIT SPECTROSCOPY

4.1 Observations and data reduction

The spectroscopic observations of the sample galaxies were carried out in three runs at ESO in La Silla (Chile) on December 2002, 9-12 (run 1), September 2003, 26-28 (run 2), and January 2005, 25 (run 3).

In run 1 and 2 the 3.6-m ESO Telescope mounted the EFOSC2 spectrograph. The grism No. 9 with 600 grooves mm^{-1} was used in combination with the 1.0 arcsec $\times$ 5.0 arcmin slit and the No. 40 Loral/Lesser CCD with 2048×2048 pixels of $15 \times 15\ \mu$m^2. A 2×2 pixel binning was adopted. The wavelength range between 4700 and 6770 Å was covered with a reciprocal dispersion of 1.98 Å pixel^{-1} after pixel binning. This guarantees an adequate oversampling of the instrumental broadening function. Indeed, the instrumental dispersion, obtained by measuring the width of emission lines of a comparison spectrum after the wavelength calibration, was 5.10 Å (FWHM). This corresponds to $\sigma_{\rm inst} \sim 110$ km s^{-1} at 5735 Å. The spatial scale was 0.314 arcsec pixel^{-1} after pixel binning.

In run 3 the New Technology Telescope mounted the ESO Multi-Mode Instrument (EMMI) in red medium-dispersion spectroscopic (REMD) mode. It used the grating No. 6 with 1200 grooves mm^{-1} with a 1.0 arcsec $\times$ 5.5 arcmin slit. The detector was a mosaic of the No. 62 and No. 63 MIT/LL CCDs. Each CCD has 2048×4096 pixels of $15 \times 15\ \mu$m^2. We adopted a 2×2 pixel

[2] The updated version of this code is available on http://cow.physics.wisc.edu∼craigm/idl/idl.html
[3] Interactive Data Language

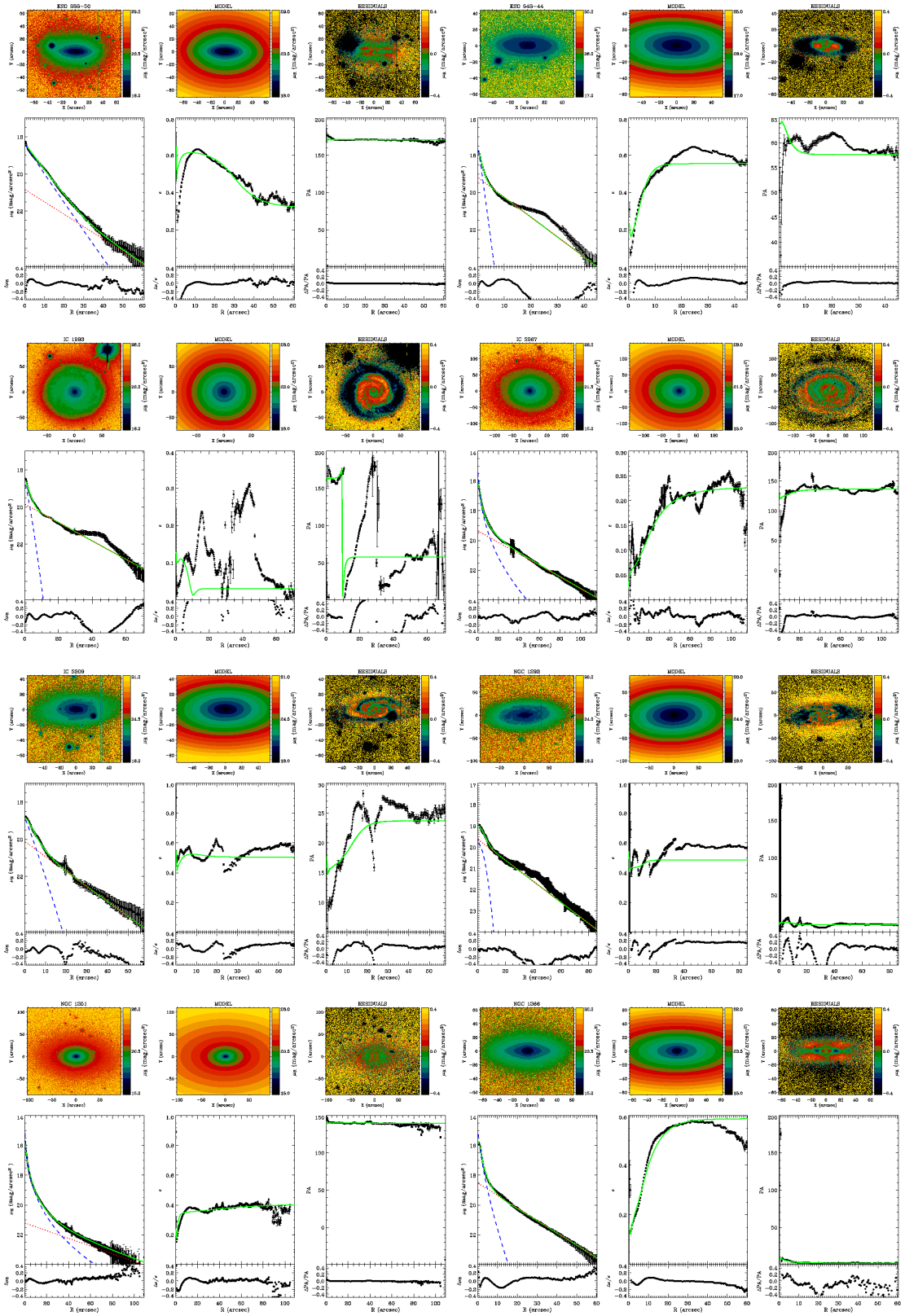

Figure 1. Two-dimensional photometric decomposition of the sample galaxies. Upper panels (from left to right): Map of the observed, modeled and residual (observed-modeled) surface-brightness distribution of the galaxy. The surface-brightness range of each image is indicated at the right of the panel. All images were rotated to have the galaxy major axis parallel to rows. In each panel the spatial coordinates with respect to the galaxy centre are given in arcsec. Lower panels (from left to right): Ellipse-averaged radial profile of surface-brightness, position angle, and ellipticity measured in the observed (dots with error-bars) and modeled image (solid line). The dashed and dotted lines represent the intrinsic surface-brightness contribution of the bulge and disc, respectively. The difference between the ellipse-averaged radial profiles extracted from the observed and modeled images is also shown.

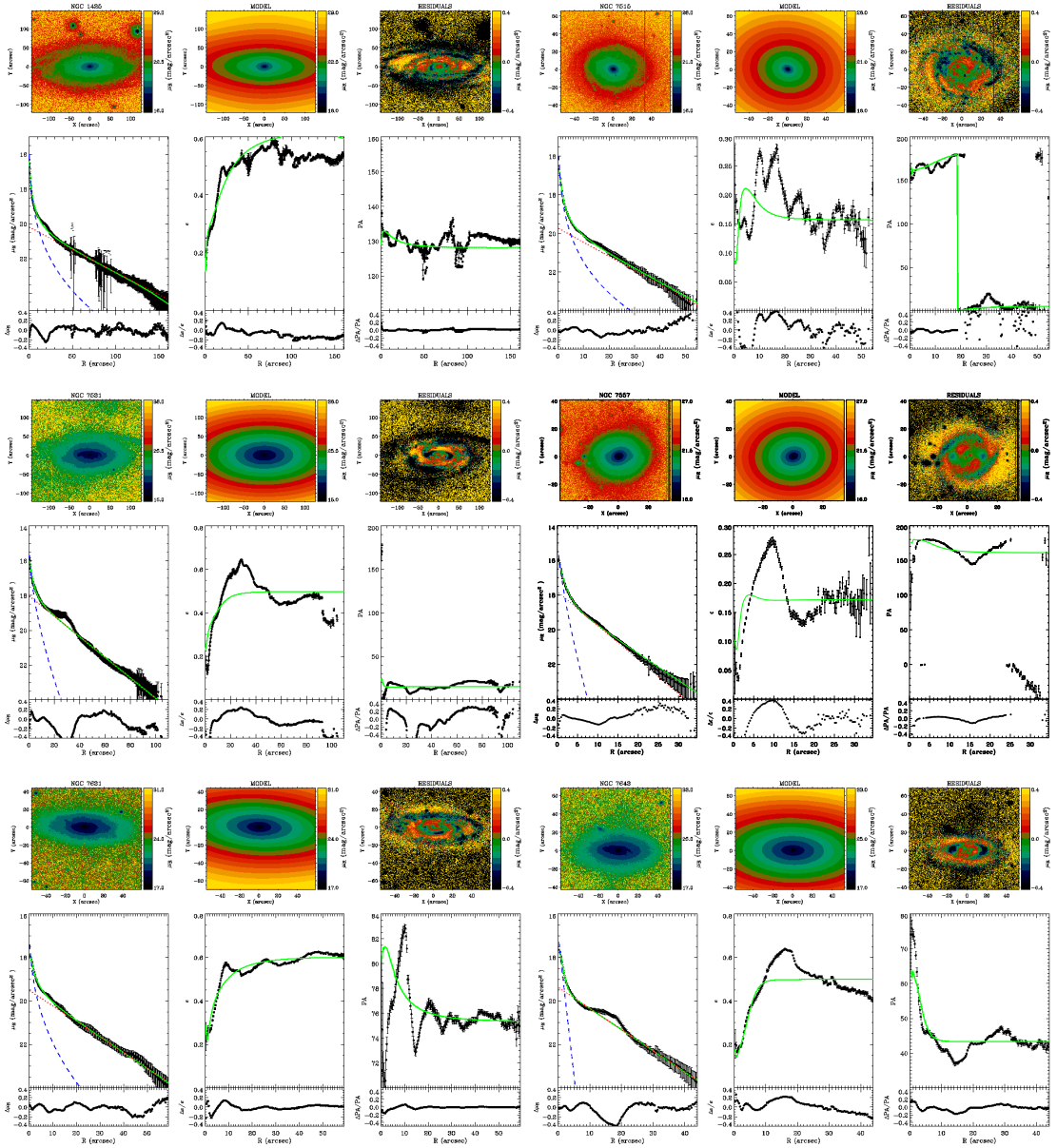

Figure 1 – *continued*

binning. It yielded a wavelength coverage between about 4850 Å and 5490 Å with a reciprocal dispersion of 0.40 Å pixel^{-1} after pixel binning. The instrumental dispersion is 1.00 Å (FWHM) corresponding to $\sigma_{\rm inst} \sim 25$ km s^{-1} at 5170 Å. The spatial scale was 0.332 arcsec pixel^{-1} after pixel binning.

Table 2. The photometric parameters of bulge and disc in the sample galaxies. The columns show the following: (2) the effective surface brightness of the bulge; (3) effective radius of the bulge; (4) shape parameter of the bulge; (5) axial ratio of the bulge isophotes; (6) position angle of the bulge major-axis; (7) central surface brightness of the disc; (8) scale length of the disc; (9) axial ratio of the disc isophotes; (10) position angle of the disc major-axis; (11) bulge-to-total luminosity ratio; (12) radius where the bulge and the disc surface brightness are the same; (13) total absolute magnitude of the bulge.

Galaxy	$\mu_{\rm e}$ (mag/arcsec^2)	$r_{\rm e}$ (arcsec)	n	$q_{\rm b}$	PA$_{\rm b}$ ($^\circ$)	μ_0 (mag/arcsec^2)	h (arcsec)	$q_{\rm d}$	PA$_{\rm d}$ ($^\circ$)	B/T	$r_{\rm db}$ (arcsec)	m_R (mag)
(1)	(2)	(3)	(4)	(5)	(6)	(7)	(8)	(9)	(10)	(11)	(12)	(13)
ESO 358-50	20.00 ± 0.05	11.63 ± 0.48	1.03 ± 0.03	0.36 ± 0.01	171.25 ± 2.85	20.57 ± 0.05	16.12 ± 0.67	0.68 ± 0.02	170.62 ± 2.84	0.63 ± 0.10	27.0 ± 1.1	-17.83 ± 0.22
ESO 548-44	19.59 ± 0.05	1.72 ± 0.07	0.94 ± 0.02	0.79 ± 0.02	65.72 ± 3.19	19.62 ± 0.05	10.02 ± 0.42	0.44 ± 0.01	57.64 ± 2.84	0.05 ± 0.01	2.2 ± 0.5	-16.23 ± 0.22
IC 1993	19.21 ± 0.04	3.22 ± 0.09	0.82 ± 0.01	0.87 ± 0.02	163.01 ± 0.41	18.91 ± 0.03	21.70 ± 0.55	0.97 ± 0.02	57.87 ± 2.34	0.03 ± 0.01	4.8 ± 0.6	-15.93 ± 0.21
IC 5267	18.76 ± 0.02	9.01 ± 0.17	2.56 ± 0.06	0.94 ± 0.02	123.51 ± 2.05	18.86 ± 0.02	27.46 ± 0.51	0.77 ± 0.01	136.63 ± 2.36	0.25 ± 0.04	14.0 ± 0.7	-20.30 ± 0.20
IC 5309	20.80 ± 0.06	5.41 ± 0.24	0.93 ± 0.02	0.44 ± 0.01	15.28 ± 2.62	20.40 ± 0.06	13.34 ± 0.68	0.49 ± 0.01	23.71 ± 3.01	0.17 ± 0.02	7.0 ± 0.9	-18.44 ± 0.23
NGC 1292	20.77 ± 0.04	4.71 ± 0.14	0.52 ± 0.01	0.57 ± 0.01	14.60 ± 2.67	19.82 ± 0.03	21.62 ± 0.59	0.51 ± 0.01	10.06 ± 2.80	0.03 ± 0.01	...	-15.77 ± 0.21
NGC 1351	19.87 ± 0.03	13.14 ± 0.33	3.39 ± 0.07	0.64 ± 0.01	140.53 ± 2.60	21.20 ± 0.02	41.51 ± 0.87	0.59 ± 0.01	139.61 ± 2.44	0.53 ± 0.12	32.5 ± 1.2	-19.71 ± 0.20
NGC 1366	18.00 ± 0.04	2.59 ± 0.07	1.50 ± 0.03	0.80 ± 0.01	5.38 ± 2.40	19.07 ± 0.03	12.81 ± 0.32	0.41 ± 0.01	2.08 ± 2.32	0.20 ± 0.06	5.0 ± 0.4	-18.45 ± 0.21
NGC 1425	21.66 ± 0.03	15.52 ± 0.40	3.70 ± 0.07	0.71 ± 0.01	133.42 ± 2.71	20.83 ± 0.02	41.37 ± 0.87	0.34 ± 0.01	127.85 ± 2.42	0.18 ± 0.06	15.0 ± 1.3	-19.09 ± 0.20
NGC 7515	20.88 ± 0.04	8.14 ± 0.24	5.09 ± 0.10	0.76 ± 0.01	162.23 ± 1.56	19.55 ± 0.03	14.68 ± 0.40	0.84 ± 0.02	8.20 ± 2.50	0.27 ± 0.07	6.0 ± 0.6	-20.25 ± 0.20
NGC 7531	18.24 ± 0.02	4.58 ± 0.08	1.70 ± 0.04	0.66 ± 0.01	14.02 ± 2.49	17.92 ± 0.02	18.15 ± 0.34	0.50 ± 0.01	15.00 ± 2.45	0.10 ± 0.02	5.0 ± 0.4	-18.53 ± 0.20
NGC 7557	17.06 ± 0.05	1.31 ± 0.05	1.38 ± 0.03	0.82 ± 0.01	180.46 ± 3.09	17.45 ± 0.04	5.46 ± 0.18	0.87 ± 0.02	172.667 ± 3.16	0.16 ± 0.04	2.1 ± 0.9	-19.34 ± 0.21
NGC 7631	21.34 ± 0.05	7.01 ± 0.26	2.68 ± 0.06	0.63 ± 0.01	83.40 ± 2.55	19.67 ± 0.04	14.90 ± 0.50	0.38 ± 0.01	75.06 ± 2.55	0.12 ± 0.04	3.0 ± 0.8	-19.27 ± 0.21
NGC 7643	19.08 ± 0.05	1.37 ± 0.05	1.01 ± 0.03	0.75 ± 0.02	63.30 ± 3.50	19.73 ± 0.05	10.97 ± 0.46	0.50 ± 0.01	43.32 ± 2.86	0.05 ± 0.01	2.5 ± 0.5	-17.89 ± 0.22

We obtained 2×45-minutes spectra for all the sample galaxies in run 1 and 2. In run 3 we obtained new 30-minutes spectra of ESO 358-50, ESO 548-44, NGC 1292, and IC 1993 which turned out to have a central velocity dispersion lower than 100 $\mathrm{km\ s^{-1}}$.At the beginning of each exposure, the slit was positioned on the galaxy nucleus using the guiding camera. Then it was aligned along the galaxy major axis, according to the position angle given in Table 1. During the three observing runs, we took spectra of several giant stars which were selected from Worthey et al. (1994) to be used as templates in measuring the stellar kinematics and line strength indices. In run 1 and 2 we observed HR 296 (K0III-IV), HR 489 (K3III), HR 2429 (K1III), HR 2503 (K4III), HR 2701 (K0III), HR 2970 (K0III), HR 3145 (K2III), HR 3418 (K2III), HR 7149 (K2III), HR 7317 (K3III), and HR 7430 (G9III). In run 3 we observed HR 294 (K0III), HR 510 (G8III), HR 1318 (K3III), and HR 2035 (G8III). Additionally, we observed three spectrophotometrical standard stars in order to flux-calibrate the galaxy and line strength standard stars before the line indices were measured. A spectrum of the comparison helium-argon arc lamp was taken before and/or after each target exposure to allow an accurate wavelength calibration. The value of the seeing FWHM during the galaxy exposures ranged between 0.5 and 1.3 arcsec as measured by fitting a two-dimensional Gaussian to the guide star.

All the spectra were bias subtracted, flat-field corrected, cleaned of cosmic rays, and wavelength calibrated using standard `IRAF` routines. The bias level was determined from the bias frames obtained during the observing nights to check the CCD status. The flat-field correction was performed by means of both quartz lamp and twilight sky spectra (which were normalized and divided into all the spectra) to correct for pixel-to-pixel sensitivity variations and large-scale illumination patterns due to slit vignetting. Cosmic rays were identified by comparing the counts in each pixel with the local mean and standard deviation (as obtained from Poisson statistics by taking into account the gain and read-out noise of the detector) and then corrected by interpolating over. The residual cosmic rays were corrected by manually editing the spectra. Each spectrum was rebinned using the wavelength solution obtained from the corresponding arc-lamp spectrum. We checked that the wavelength rebinning had been done properly by measuring the difference between the measured and predicted wavelengths for the brightest night-sky emission lines in the observed spectral range (Osterbrock et al. 1996). The resulting accuracy in the wavelength calibration is better than 5 $\mathrm{km\ s^{-1}}$. All the spectra were corrected for CCD misalignment following Bender, Saglia & Gerhard (1994, BSG94). The spectra obtained for the same galaxy in the same run were co-added using the center of the stellar continuum as reference. This allowed to improve the S/N of the resulting two-dimensional spectrum. In such a spectrum, the contribution of the sky was determined by interpolating a one-degree polynomium along the outermost 20 arcsec at the two edges of the slit, where the galaxy light was negligible, and then subtracted. A sky subtraction better than 1% was achieved. A one-dimensional spectrum was obtained for each kinematical template star as well as for each flux standard star. The spectra of the kinematical templates were deredshifted to laboratory wavelengths.

4.2 Measuring stellar kinematics and line-strength indices

We measured the stellar kinematics from the galaxy absorption features present in the wavelength range and centered on the Mg line triplet ($\lambda\lambda$ 5164, 5173, 5184 Å) by applying the Fourier Correlation Quotient method (Bender 1990) as done by BSG94. The spectra were rebinned along the dispersion direction to a natural logarithmic scale, and along the spatial direction to obtain a $S/N \geqslant 40$ per resolution element. For run 3 it was necessary to average the whole spectra obtaining a one-dimensional spectrum in order to achieve the desired S/N. In few spectra of run 1 and 2 the S/N decreases to 10 at the outermost radii. To measure the stellar kinematics of the sample galaxies we adopted HR 296, HR 2429, and HR 2701 as kinematical templates for runs 1 and 2 and HR 296 and HR 510 for run 3. We considered the wavelength range 4817-6503 Å in runs 1 and 2 and 5167-5378 Å in run 3 around the redshifted Mg lines of the galaxies. We derived for each galaxy spectrum, the line-of-sight velocity distribution (LOSVD) along the slit and measured the radial velocity v and velocity dispersion σ. At each radius, they have been derived by fitting the LOSVD with a Gaussian. The errors on the LOSVD moments were derived from photon statistics and CCD read-out noise, calibrating them by Monte Carlo simulations as done by BSG94. In general, errors are in the range 5–20 $\mathrm{km\ s^{-1}}$, becoming larger in the outer regions of some galaxies where $10 \leqslant S/N \leqslant 20$. These errors do not take into account the possible systematic effects arising from template mismatch. The measured stellar kinematics are plotted in Fig. A1 and given in Tab. B1.

Detailed measurements of kinematics is not only important to study the dynamical properties of galaxies but also to derive the line strength of the Lick indices. Following Mehlert et al. (2000), we measured the Mg, Fe, and H_β line-strength indices (as defined by Faber et al. 1985 and Worthey et al. 1994) from the flux-calibrated spectra of run 1 and 2. Spectra were rebinned in the dispersion direction as well as in the radial direction as before. We indicate the average Iron index with $\langle\mathrm{Fe}\rangle = (\mathrm{Fe5270} + \mathrm{Fe5335})/2$ (Gorgas et al. 1990), and the newly defined Magnesium-Iron index with $[\mathrm{MgFe}]' = \sqrt{\mathrm{Mg}\,b\,(0.72 \times \mathrm{Fe5270} + 0.28 \times \mathrm{Fe5335})}$ (Thomas et al. 2003). We convolved all the spectra with a Gaussian with a proper σ to degrade them to the fixed spectral resolution of the Lick system ($\simeq 9$ Å). No focus correction was applied because the atmospheric seeing was the dominant effect during observations (see Mehlert et al. 1998, for details). The errors on indices were derived from photon statistics and CCD read-out noise, and calibrated by means of Monte Carlo simulations. We calibrated our measurements to the Lick system using the stars from Worthey et al. (1994) we observed in run 1 and 2. A well known problem when deriving age and metallicity of galaxy stellar populations is the contamination of the H_β index by the H_β emission line. To address this issue we adopted the code GANDALF (Gas AND Absorbtion Line fitting) to fit the galaxy spectra with synthetic population models as done by Sarzi et al. (2006). The models were built with different templates from the stellar libraries by Bruzual & Charlot (2003) and Tremonti et al. (2004). We adopted the Salpeter initial mass function (Salpeter 1955), ages ranging between 1 Myr and 10 Gyr, and metallicities between 1 and 2.5 $(Z/\mathrm{H})_\odot$. The spectral resolution of the stellar templates (FWHM$\sim$ 3 Å) was degraded to match that our galaxy spectra. We simultaneously fitted the observed spectra using emission lines in addition to the stellar templates. The H_β emission line was detected ($S/N > 3$) in NGC 1292, NGC 7531, NGC 7631, NGC 7643, IC 5267, IC 5309. The equivalent with of H_β emission line was ranging from 0 to 4 Å depending on the galaxy and radius (Tab. B1). The emission line was subtracted from the observed spectrum and we measured the H_β line-strength index from the resulting H_β absorption line.

The measured values for the line-strength indices for the stars in common with Worthey et al. (1994) are shown in Fig. 2. The

Table 3. The central values (averaged over 0.3 $r_{\rm e}$) of the velocity dispersion and line-strength of the measured Lick indices.

Galaxy	σ (km s^{-1})	$\langle$Fe$\rangle$ (Å)	[MgFe]$'$ (Å)	Mg$_2$ (mag)	Mg$_b$ (Å)	H$_\beta$ (Å)
(1)	(2)	(3)	(4)	(5)	(6)	(7)
ESO 358-50	39.0 ± 3.4	2.45 ± 0.24	2.60 ± 0.05	0.004 ± 2.719	2.72 ± 0.18	2.35 ± 0.15
ESO 548-44	63.8 ± 7.0	2.71 ± 0.52	2.91 ± 0.30	0.190 ± 0.012	3.04 ± 0.40	2.01 ± 0.35
IC 1993	182.8 ± 15.0	2.71 ± 0.30	2.94 ± 0.10	0.176 ± 0.008	3.07 ± 0.23	2.05 ± 0.21
IC 5267	203.1 ± 15.1	3.05 ± 0.28	3.80 ± 0.14	0.281 ± 0.007	4.65 ± 0.26	1.58 ± 0.17
IC 5309	108.0 ± 15.9	2.01 ± 0.26	2.15 ± 0.05	0.131 ± 0.005	2.27 ± 0.20	2.62 ± 0.17
NGC 1292	31.7 ± 3.4	1.63 ± 0.61	1.67 ± 0.23	0.103 ± 0.011	1.61 ± 0.46	2.72 ± 0.41
NGC 1351	193.9 ± 11.0	2.85 ± 0.23	3.67 ± 0.07	0.279 ± 0.005	4.66 ± 0.17	1.60 ± 0.14
NGC 1366	175.8 ± 9.2	3.13 ± 0.17	3.67 ± 0.04	0.263 ± 0.004	4.23 ± 0.13	1.78 ± 0.11
NGC 1425	126.9 ± 12.4	2.59 ± 0.21	3.06 ± 0.05	0.214 ± 0.004	3.52 ± 0.16	1.72 ± 0.14
NGC 7515	157.7 ± 15.6	2.73 ± 0.27	3.15 ± 0.10	0.209 ± 0.006	3.56 ± 0.22	2.04 ± 0.17
NGC 7531	132.8 ± 10.0	2.75 ± 0.17	2.94 ± 0.04	0.199 ± 0.004	3.15 ± 0.14	2.00 ± 0.11
NGC 7557	104.6 ± 15.0	2.58 ± 0.21	2.78 ± 0.04	0.176 ± 0.004	2.91 ± 0.16	2.80 ± 0.13
NGC 7631	155.5 ± 15.8	2.45 ± 0.37	2.83 ± 0.14	0.170 ± 0.008	3.20 ± 0.28	1.93 ± 0.24
NGC 7643	116.9 ± 13.0	2.18 ± 0.25	2.46 ± 0.06	0.141 ± 0.005	2.71 ± 0.19	2.88 ± 0.17

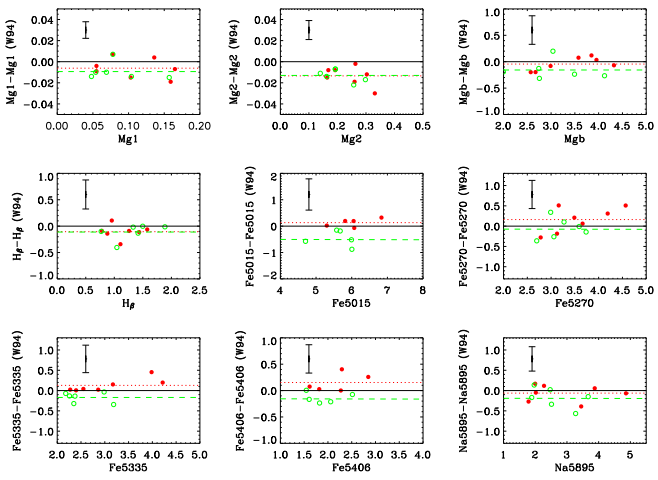

Figure 2. Comparison of the values of the line-strength indices of the stars in common with Worthey et al. (1994) (W94). The error bars in the upper left corner of each panel indicate the median errors of the measurements. Negligible offsets for all indices were obtained by assuming the the straight line averaging the data in run 1 (filled red dots) and 2 (empty green dots).

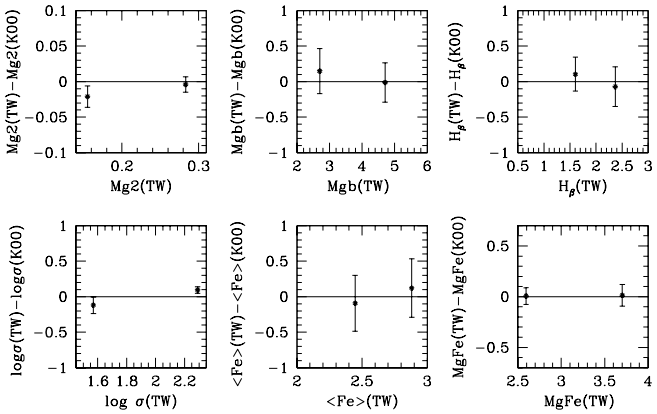

Figure 3. Comparison of the values of the central velocity dispersion and line-strength indices we and Kuntschner (2000) (K00) measured for NGC 1351 and ESO 358-G50. Velocity dispersions are given in km s^{-1}, Mg$_2$ in mag, and all the other line-strength indices in Å.

agreement is good within the errors for all the indices and we did not apply any zero-point correction.

Kuntschner (2000) measured the central velocity dispersion and line-strength indices for NGC 1351 and ESO 358-G50. The comparison is shown in Fig. 3. All the values are consistent with ours within 3σ. The measured values of H$_\beta$, [MgFe]$'$, $\langle$Fe$\rangle$, Mg$_b$, and Mg$_2$ for all the sample galaxies are plotted in Fig. 4 and listed in Tab. B1.

5 LINE-STRENGTH INDICES: CENTRAL VALUES

Central values of velocity dispersion σ, Mg$_b$, Mg$_2$, H$_\beta$, $\langle$Fe$\rangle$, and [MgFe]$'$ line-strength indices were derived from the major-axis profiles. The data points inside $0.3\ r_{\rm e}$ were averaged adopting a relative weight proportional to their S/N. The resulting values are listed in Tab. 3.

The correlations between the velocity dispersion and Mg$_2$, H$_\beta$, and $\langle$Fe$\rangle$ line-strength indices for the sample galaxies are plotted in Fig. 5. They were extensively studied for early-type galaxies (see Fisher et al. 1996; Bernardi et al. 1998; Jørgensen 1999a; Kuntschner 2000; Moore et al. 2002; Mehlert et al. 2003; Rampazzo et al. 2005; Sánchez-Blázquez et al. 2006; Collobert et al. 2006; Annibali et al. 2007). In Fig. 5 we also plotted for comparison the fitted correlations to different sample of elliptical/early-type galaxies and bulges.

The Mg$_2$ line-strength index is generally adopted as the tracer of the α elements giving an estimate of the enrichment, while σ is related with the gravitational potential. In elliptical and S0 galaxies the Mg$_2$−σ correlation shows that more massive galaxies host a more metal rich stellar population (see Idiart et al. 1996; Bernardi et al. 1998; Jørgensen 1999a; Mehlert et al. 2003). For

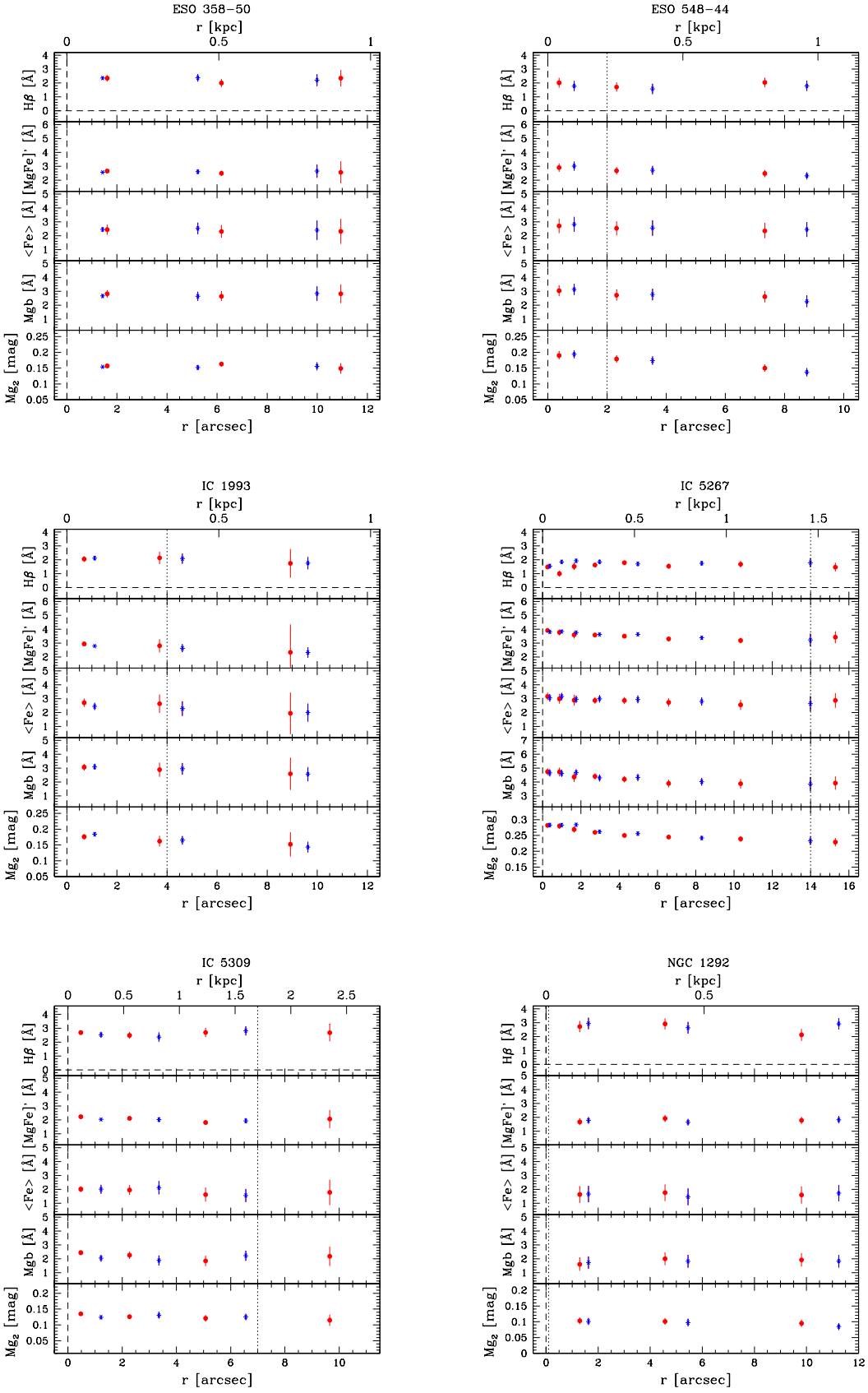

Figure 4. The line-strength indices measured along the major axes of the sample galaxies. From top to bottom: folded radial profiles of H_β, $[MgFe]'$, $\langle Fe \rangle$, Mg_b, and Mg_2. Asterisks and dots refer to the two sides (est/west) of the galaxy. The vertical dashed line indicates the radius(r_{db}) where the surface-brightness contributions of the bulge and disc are equal.

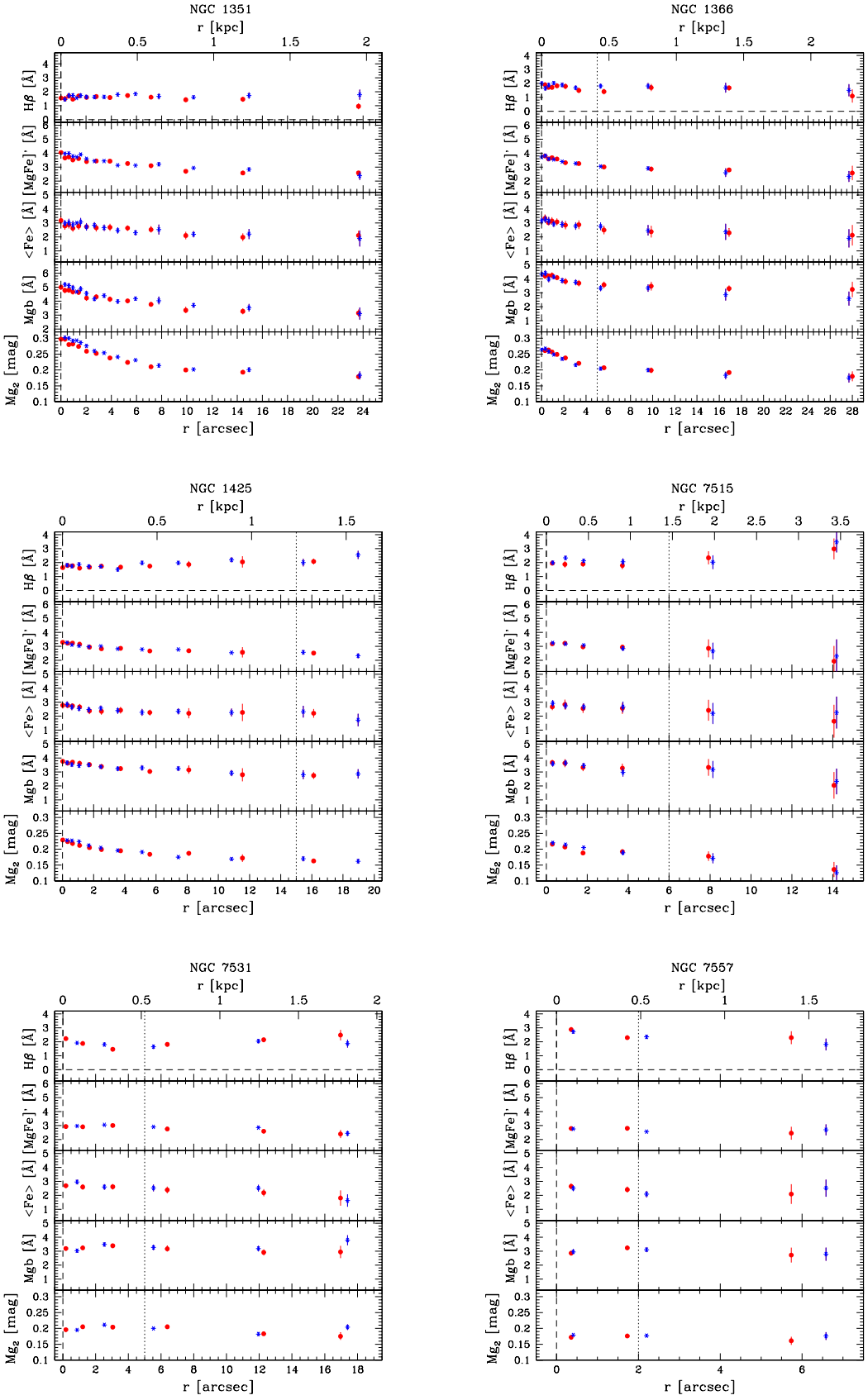

Figure 4 – *continued*

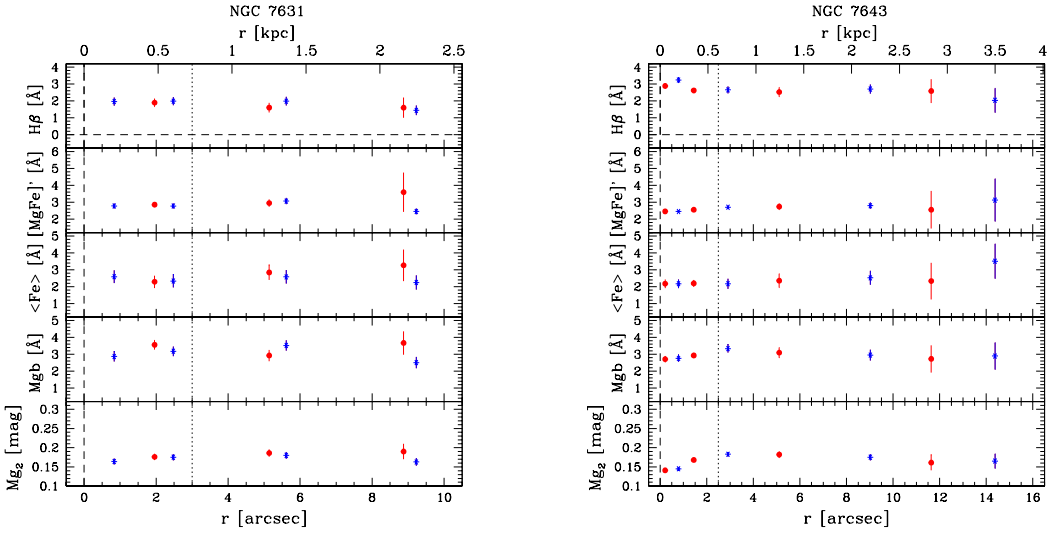

Figure 4 – *continued*

bulges we measured a similar trend to that found by Jablonka et al. (1996), Prugniel et al. (2001), and Ganda et al. (2007). In agreement with Ganda et al. (2007) we also found that the spirals lie below the $\mathrm{Mg}_2-\sigma$ relation defined by the elliptical and early-type galaxies (Jørgensen 1999a).

Although the correlation between $\langle\mathrm{Fe}\rangle$ and σ was predicted by models of the dissipative collapse (e.g., Kodama et al. 1998), it was not found to be very tight in early-type galaxies (Fisher et al. 1996; Jørgensen 1999a; Trager et al. 1998; Mehlert et al. 2003) except for those studied by Kuntschner (2000). On the other hand, the $\langle\mathrm{Fe}\rangle-\sigma$ relation is well defined for spiral bulges (Idiart et al. 1996; Prugniel et al. 2001; Proctor & Sansom 2002). The fitted slope is slightly steeper that the one traced for elliptical/early-type galaxies (Jørgensen 1999a) and consistent with the relation by Proctor & Sansom (2002).

We also found a tight anti-correlation between H_β and σ. For large values of σ our measurements are consistent with previous results by Jørgensen (1999a) and Ganda et al. (2007). At low σ our fit follows closer the relation by Jørgensen (1999a) due to the presence of S0-Sa galaxies in our sample. Nevertheless, the spiral galaxies are lying on the fitted line of the well selected Sb-Sc sample given by Ganda et al. (2007). The comparison with Jørgensen (1999a) could be affected by the possible contamination of their H_β line-strength indices by the H_β emission line due to the presence of a young stellar component.

Young stellar population is often associated to dusts (e.g., Peletier et al. 2007). The dust structure is clearly visible in the residual maps of the two-dimensional bulge-disc decompositions (Fig. 1). No correlation is found between dust and central values of the line-strength indices. But, the dust is located at larger radii than the regions mapped by the spectra (Fig. 4). Only for NGC 7515 and NGC 7643 the outer radial bins of spectra cover a portion of the dust features observed in the residual maps. The strong H_β emission line detected at these radii is indicating the presence a local young stellar population. But, this is not enough to drive a general conclusion about the correlation of dust and stellar populations in the sample galaxies.

6 AGES, METALLICITIES, AND α/FE ENHANCEMENT:CENTRAL VALUES

From the central line-strength indices we derived the mean ages, total metallicities, and total α/Fe enhancements of the stellar populations in the center of the sample bulges by using the stellar population models by Thomas et al. (2003). These models predict the values of the line-strength indices for a single stellar population as function of the age, metallicity and $[\alpha/\mathrm{Fe}]$ ratios.

The distribution of the central H_β and $[\mathrm{MgFe}]'$ with the stellar population models by Thomas et al. (2003) is shown in Fig. 6 (left panel). The models are plotted for two fixed $[\alpha/\mathrm{Fe}]$ ratios (0 and 0.5 dex) corresponding to stellar populations with solar and super-solar α/Fe enhancements, respectively. In this parameters space the mean age and total metallicity appear to be almost insensitive to the variations of the α/Fe enhancement. The distribution of the central Mg_b and $\langle\mathrm{Fe}\rangle$ with the stellar population models by Thomas et al. (2003) is shown in Fig. 6 (right panel). The models are plotted for two fixed ages (3 and 12 Gyr) corresponding to intermediate-age and old stellar populations, respectively. In this parameters space the α/Fe enhancement and total metallicity appear to be almost insensitive to the variations of age. Central age, metallicity and total α/Fe enhancement of each bulge were derived by a linear interpolation between the model points using the iterative procedure described in Mehlert et al. (2003). The derived values and their corresponding errors are listed in Tab. 4. The histograms of their number distribution are plotted in Fig. 7. Even though the number of galaxies does not allow us to trace a firm statistical conclusion, three classes of objects were identified. according to their age and metallicity. A similar result was found by Moorthy & Holtzman (2006). The young bulges are scattered about an average age of 2 Gyr with hints of star formation as shown by the presence of the H_β emission line in their spectra. The intermediate-age bulges spans the age range between 4 and 8 Gyr. They are characterized by solar metallicity ($[Z/\mathrm{H}] = 0.0$ dex). Finally, the old bulges have a narrow distribution in age around 10 Gyr and high metallicity ($[Z/\mathrm{H}] = 0.30$ dex). Kuntschner (2000) and Mehlert et al. (2003) found that elliptical galaxies in Fornax and Coma clusters are on average older and more metal rich than S0 galaxies.

[h!]

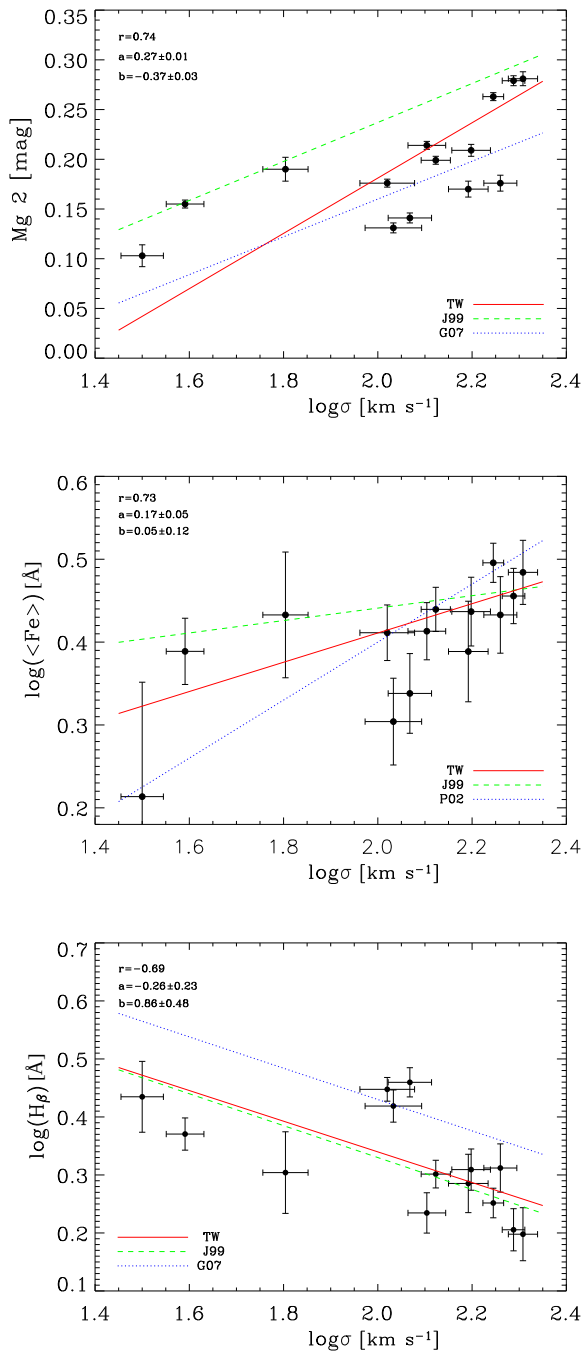

Figure 5. Central value of line strength indices Mg_2 (upper panel), $\langle\mathrm{Fe}\rangle$ (central panel) and H_β versus the velocity dispersion. In each panel the solid line represents the linear regression ($y = ax + b$) through all the data points. The Pearson correlation coefficient (r) and the results of the linear fit are given. Correlations found by differents authors are shown: TW = this work, J99 = (Jørgensen 1999a), P02 = (Proctor & Sansom 2002), G07 = (Ganda et al. 2007).

Table 4. The central ages, metallicities and α/Fe enhancements of the sample bulges derived from the line-strength indices listed in Tab. 3 using the stellar population models by Thomas et al. (2003).

Galaxy	$[Z/\mathrm{H}]$	Age [Gyr]	$[\alpha/\mathrm{Fe}]$
(1)	(2)	(3)	(4)
ESO 358-50	-0.04 ± 0.08	2.8 ± 1.1	-0.00 ± 0.11
ESO 548-44	-0.00 ± 0.20	4.7 ± 4.6	-0.05 ± 0.17
IC 1993	0.04 ± 0.14	4.2 ± 2.8	-0.04 ± 0.13
IC 5267	0.34 ± 0.15	9.5 ± 4.2	0.18 ± 0.10
IC 5309	-0.24 ± 0.08	2.7 ± 1.3	0.05 ± 0.13
NGC 1292	-0.68 ± 0.28	4.2 ± 2.6	-0.12 ± 0.22
NGC 1351	0.25 ± 0.09	9.9 ± 3.3	0.23 ± 0.08
NGC 1366	0.39 ± 0.08	5.1 ± 1.7	0.11 ± 0.05
NGC 1425	-0.07 ± 0.07	10.3 ± 2.9	0.08 ± 0.10
NGC 7515	0.17 ± 0.13	4.0 ± 2.0	0.09 ± 0.11
NGC 7531	0.01 ± 0.06	4.8 ± 1.5	-0.03 ± 0.07
NGC 7557	0.27 ± 0.08	1.5 ± 0.2	0.06 ± 0.09
NGC 7631	-0.10 ± 0.14	6.9 ± 3.3	0.07 ± 0.17
NGC 7643	0.05 ± 0.06	1.8 ± 0.2	0.14 ± 0.13

Thomas & Davies (2006) did not observe any correlation between the age and metallicity of the bulge stellar population and galaxy morphology. This was interpreted as an indication of independent evolution of the stellar populations of the bulges and discs. In the sample studied by Peletier et al. (2007) the early-type spirals often show young stellar populations in their central regions, but there are also objects that are as old as the oldest ellipticals. Young central populations are seen in all the late-type spirals of Ganda et al. (2007). The correlation between the morphological type (col. 3, Tab. 1) and the age, metallicity and α/Fe enhancement of our sample galaxies are shown in Fig. 9. Although the correlations are not statistically very strong (in particular for the α/Fe enhancement), the elliptical and S0 galaxies ($T < 0$) are older and more metal rich than the spirals ($T > 0$).

Most of the sample bulges display Solar α/Fe enhancements with the median of the distribution at ($[\alpha/\mathrm{Fe}] = 0.07$). A few have a central super-solar enhancement ($[\alpha/\mathrm{Fe}] = 0.3$). These values are similar to those found for the elliptical galaxies in cluster (Peletier 1989; Jørgensen 1999b; Trager et al. 2000; Kuntschner 2000; Kuntschner et al. 2001) and imply a star-formation timescale ranging from 1 to 5 Gyr.

Age, metallicity, and α/Fe enhancement correlate with velocity dispersion (Fig. 8). In early-type galaxies the metallicity and α/Fe enhancement are well correlated with the central velocity dispersion, while the correlation is less evident with age (Mehlert et al. 2003; Sánchez-Blázquez et al. 2006; Denicoló et al. 2005). In our bulges both the metallicity and α/Fe enhancement correlate with the velocity dispersion and this is probably driving the correlation observed between the metallicity and α/Fe enhancement (Fig. 10). Age is mildly correlated with velocity dispersion (Fig. 8), and α/Fe enhancement (Fig.10). Recently, Thomas & Davies (2006) proved that these correlations are tighter when the age estimation is based on bluer Balmer line-strenght indices instead of H_β. We conclude that the more massive bulges of our sample galaxies are older, more metal rich and characterized by a fast star formation. Since we did not found any correlation with galaxy morphology we exclude a strong interplay between the bulge and the disc components.

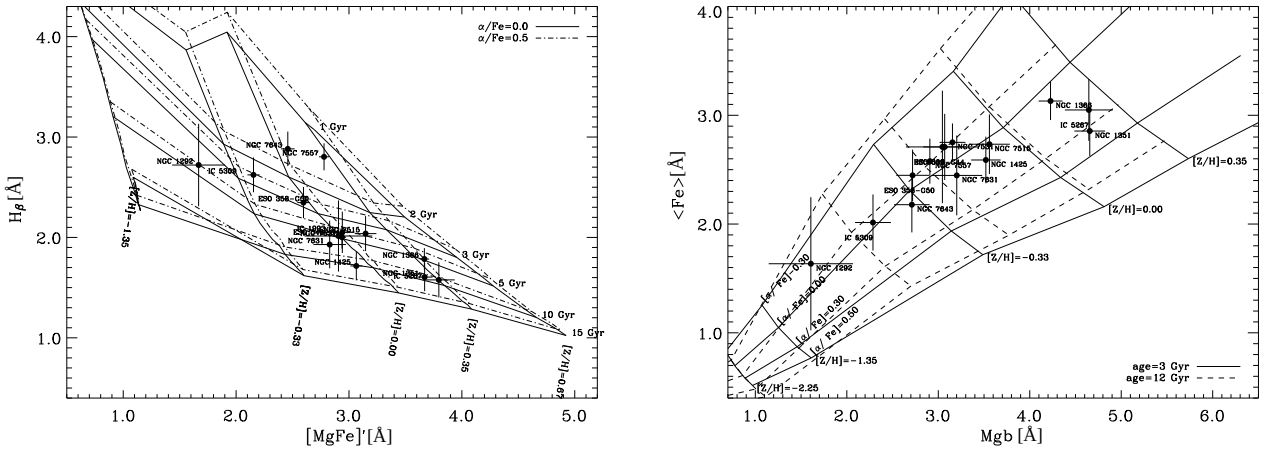

Figure 6. The distribution of the central values of H_β and $[MgFe]'$ indices (left panel) and $\langle Fe\rangle$and Mg_b indices (right panel) averaged over $0.3\ r_e$ for the 15 sample galaxies . The lines indicate the models by Thomas et al. (2003). In the left panel the age-metallicity grids are plotted with two different α/Fe enhancements: $[\alpha/Fe] = 0.0$ dex (continuous lines) and $[\alpha/Fe] = 0.5$ dex (dashed lines). In the right panel the $[\alpha/Fe]$-metallicity grids are plotted with two different ages: 3 Gyr (continuous lines) and 12 Gyr (dashed lines).

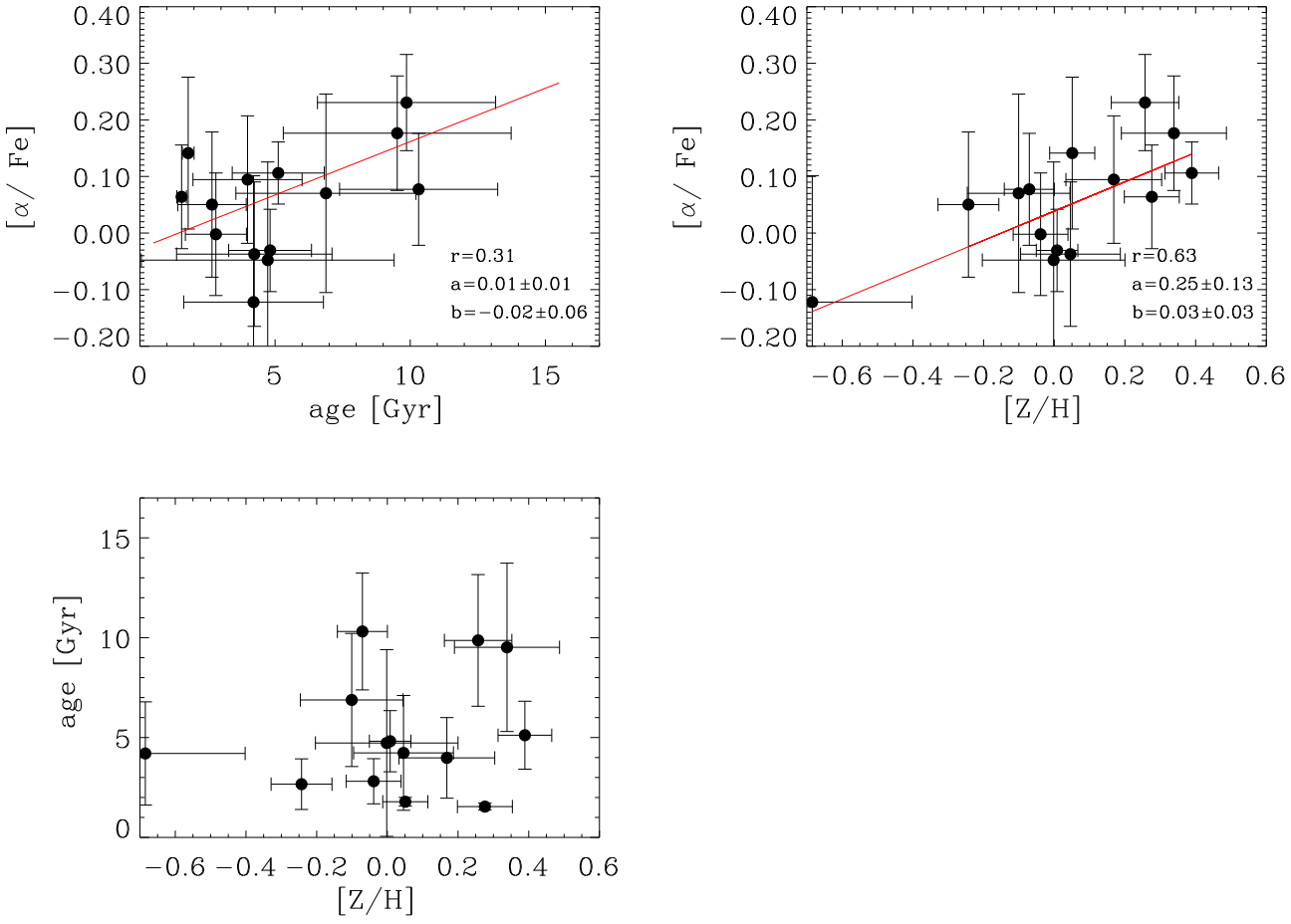

Figure 10. The central ages, metallicities and α/Fe enhancements of the sample bulges listed in Tab.4. In each panel the solid line represents the linear regression ($y = ax + b$) through all the data points. The Pearson correlation coefficient (r) and the results of the linear fit are given.

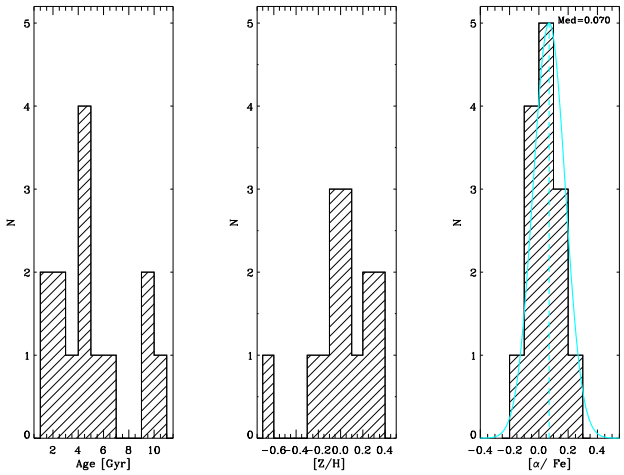

Figure 7. Distribution of age (left panel), metallicity (central panel) and $[\alpha/\mathrm{Fe}]$ enhancement (right panel) for the central regions of the sample galaxies. The solid line in the right panel represents a Gaussian centered in the median value$[\alpha/\mathrm{Fe}] = 0.07$ of distribution. Its $\sigma = 0.11$ is approximated by the value containing the 68% of the objects of the distribution.

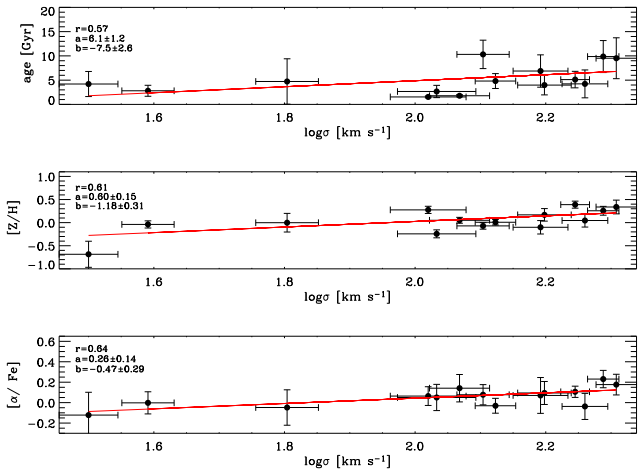

Figure 8. Correlation between the central values of age, metallicity and α-enhancement with central velocity dispersion of the sample galaxies. In each panel the solid line represents the linear regression ($y = ax + b$) through all the data points. The Pearson correlation coefficient (r) and the results of the linear fit are given.

7 AGES, METALLICITIES, AND α/FE ENHANCEMENT: GRADIENTS

Different formation scenarios predict different radial trends of age, metallicity, and α/Fe enhancement. Therefore the radial gradients of the properties of the stellar populations of bulges are a key information to understand the processes of their formation and evolution.

The total metallicity of a stellar population depends only on the efficiency of the star formation and on the amount of gas transformed in star (Tinsley 1980). In the monolithic collapse scenario gas dissipation toward the galaxy centre with subsequent occurrence of star formation and blowing of galactic winds produce a steep metallicity gradient (Eggen et al. 1962; Larson 1974;

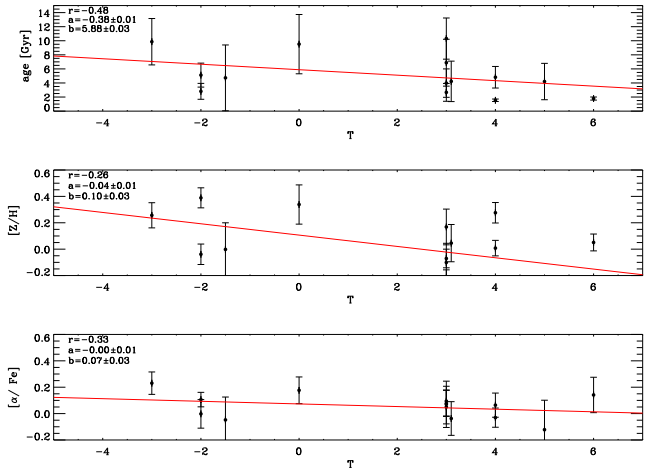

Figure 9. Correlation between the central values of age, metallicity, and α-enhancement with morphological type of the sample galaxies. In each panel the solid line represents the linear regression ($y = ax + b$) through all the data points. The Pearson correlation coefficient (r) and the results of the linear fit are given.

Arimoto & Yoshii 1987). A strong gradient in α/Fe enhancement is expected too (Ferreras & Silk 2002). The predictions for bulges forming through a long time-scale processes as dissipation-less secular evolution are more contradictory. In this scenario the bulge is formed by redistribution of disc stars. The gradients eventually present in the progenitor disk, could be either amplified since the resulting bulge has a smaller scale length than the progenitor or erased as a consequence of disc heating (Moorthy & Holtzman 2006).

An issue in measuring the gradients of age, metallicity and α/Fe enhancement in bulge, could be the contamination of their stellar population by the light coming from the underlying disc stellar component. This effect is negligible in the galaxy center but it could increase going to the outer regions of the bulge, where the light starts to be dominated by the disc component. In order to reduce the impact of disc contamination and extend as much as possible the region in which deriving gradients, we map them inside r_{bd}, the radius where the bulge and disc give the same contribution to the total surface-brightness. This is a region slightly larger than r_{e} of the galaxy (Fig. 11). Deriving gradients in the bulge dominated region with this approach, will not remove completely the contamination by the disc stellar population but it will assure always a similar degree of contamination in comparing the gradients of different galaxies.

For each galaxy, we derived the Mg_2, H_β, and $\langle\mathrm{Fe}\rangle$ line-strength indices at the radius r_{bd} (see Tab. 2). The ages, metallicities and α/Fe enhancements were derived by using the stellar population models by Thomas et al. (2003) as done for the central values.

The gradients were set as the difference between the values at centre and $r_{\mathrm{db}}$and their corresponding errors were calculated through Monte Carlo simulations taking into account the errors in the gradients and the logarithmic fit to the adopted indices. For NGC 1292 no gradients were obtained since it was not possible to estimate r_{bd}. The galaxy bulge is fainter than the disc at all radii (Fig. 1). Indeed, the surface-brightness radial profile of the galaxy could be fitted by adopting only an exponential disc (Tab. 2).

The final gradients of age, metallicity and α/Fe enhancement

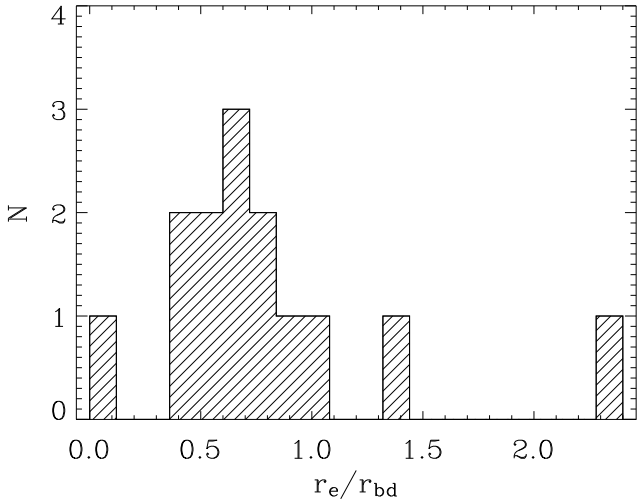

Figure 11. Distribution of the ratio between $r_{\rm e}$ and $r_{\rm bd}$; For most of the galaxies ($r_{\rm e}/r_{\rm bd}$=0.7) the gradient evaluated up to $r_{\rm bd}$ is mapping a region slightly larger than $r_{\rm e}$.

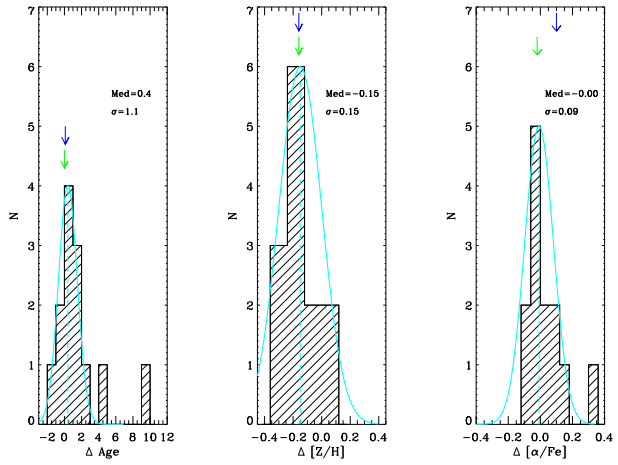

Figure 12. Distribution of the gradients of age (left panel), metallicity (central panel) and [α/Fe] enhancement (right panel) for the sample galaxies. Dashed line represents the median of the distribution and its values is reported.Solid line represents a Gaussian centered in the median value of distribution. Their σ approximated by the value containing the 68% of the objects of the distribution are reported.The green and blue arrows show the average gradient found for early-type galaxies and bulges by Mehlert et al. (2003) and Jablonka et al. (2007), respectively.

and their errors are listed in Tab. 5. In Tab. 5 we also report the age, metallicity and α/Fe enhancement gradients rescaled to a fix radius value of 1 kpc. For two galaxies (ESO 358-G50 and NGC 7531) the small values of $r_{\rm bd}$ combined with the big values of gradients give meaningless values of age extrapolated at 1 kpc and we omit them in the table. The histograms of their number distribution are plotted in Fig. 12.

Most of the sample galaxies show no gradient in age (median=0.4), in agreement with the earlier findings by Mehlert et al. (2003) and Sánchez-Blázquez et al. (2006) for the early-type galaxies, and by Jablonka et al. (2007) for bulges. Only NGC 1366 and NGC 7531 display a steep age gradient (see Fig. 12).

Negative gradients of metallicity were observed in the sample bulges. The number distribution show a clear peak at $\Delta([Z/H])=-0.15$. This was already known for the stellar populations in early-type galaxies (Proctor & Sansom 2002; Mehlert et al. 2003; Sánchez-Blázquez et al. 2006), and it has been recently found for spiral bulges too by Jablonka et al. (2007). The presence of negative gradient in the metallicity radial profile favors a scenario with bulge formation via dissipative collapse (Larson 1974).

Dissipative collapse implies strong inside-out formation that should give rise to a negative gradient in the α/Fe enhancement too (Ferreras & Silk 2002). But no gradient was measured in the [α/Fe] radial profiles for almost all the galaxies. Only 1 object of 14 are out of 3 σ of distribution (Fig. 12). All the deviations from the median values of the other objects can be explained by their errors only (Tab. 5). The same conclusion has been found by Jablonka et al. (2007) where they state that the changes in α/Fe enhancement are small and it is rather constant among their bulges.

The absence of gradients in α/Fe enhancement is not in contrast with the presence of a metallicity gradient and could be due to the different enrichment of the material fuelling the star formation.

No correlation was found between the central value and gradient of α/Fe enhancement as in Reda et al. (2007), while the central value and gradient of metallicity are related in spite of the large error-bars (Fig. 13). All these hints suggest that a pure dissipative collapse is not able to explain formation of bulges and that other phenomena like mergers or acquisition events need to be invoked (Bekki & Shioya 1999; Kobayashi & Arimoto 1999).

The peculiar gradients observed for the stellar population of the bulges of NGC 1366 and NGC 7531 suggest they have different characteristic with respect to the rest of the sample. NGC 1366 shows a steep positive age gradient (from about 5 to 11 Gyr) a strong negative metallicity gradient (from about 0.5 to 0 dex) within 5" from the centre. In this region a sharp rotation is measured while immediately further out the galaxy is almost not rotating. Moreover, the rotation in the innermost regions is opposite to that observed at large radii (Fig. A1). Even if a disc-bulge decoupling (Bertola et al. 1999; Sarzi et al. 2000; Matthews & de Grijs 2004) could give a similar kinematical signature the stellar population analysis is more suggestive of the presence counter-rotating nuclear stellar disc similar to those already observed in both elliptical (e.g., Morelli et al. 2004) and spiral galaxies (e.g., Corsini et al. 1999; Pizzella et al. 2002; Krajnović & Jaffe 2004; Emsellem et al. 2004; McDermid et al. 2006). The nuclear disc is younger than the rest of host bulge and formed by enriched material probably acquired via interaction or minor merging. The age of the stellar population of NGC 7531 rises from a central value of about 2 Gyr to 12 Gyr at 4 arcsec. Further out it decreases to 2 Gyr at 6 arcsec from the centre. Despite this change, no gradient in both metallicity and α/Fe enhancement was found. We suggest that this is due to the presence of a component which is corotating but structurally decoupled with respect to the rest of the galaxy (e.g., McDermid et al. 2006).

8 PSEUDOBULGES

The current picture of bulge demography reveals that disc galaxies can host bulges with different photometric and kinematic properties (see Kormendy & Kennicutt 2004, for a review). Classical bulges are similar to low-luminosity ellipticals and are thought to be formed by mergers and rapid collapse. Pseudobulges are disc or bar components which were slowly assembled by acquired material, efficiently transferred to galaxy centre where it formed stars. Pseudobulges can be identified according to their morphologic,

Table 5. The columns show the following: (2),(3),(4) the gradients of the ages, metallicities and α/Fe enhancements of the sample bulges derived from the central values and values at $r_{\rm bd}$ listed Tab. 2. (5),(6),(7) the gradients of the ages, metallicities and α/Fe enhancements of the sample bulges rescaled at 1 kpc. Stellar population models by Thomas et al. (2003) were used.

Galaxy	$\Delta([Z/\mathrm{H}])$	Δ(Age) [Gyr]	$\Delta([\alpha/\mathrm{Fe}])$	$\Delta([Z/\mathrm{H}])_{kpc}$	$\Delta(\mathrm{Age})_{kpc}$ [Gyr]	$\Delta([\alpha/\mathrm{Fe}])_{kpc}$
(1)	(2)	(3)	(4)	(5)	(6)	(7)
ESO 358-50	-0.15 ± 0.23	2.95 ± 3.47	-0.008 ± 0.25	-0.06 ± 0.10	1.34 ± 1.63	-0.003 ± 0.11
ESO 548-44	-0.01 ± 0.35	1.04 ± 10.80	-0.078 ± 0.26	-0.05 ± 1.44	...	-0.325 ± 1.02
IC 1993	-0.14 ± 0.26	0.20 ± 4.30	0.098 ± 0.23	-0.35 ± 0.62	0.51 ± 11.09	0.251 ± 0.63
IC 5267	-0.22 ± 0.21	-0.76 ± 7.77	-0.024 ± 0.20	-0.15 ± 0.13	-0.52 ± 5.29	-0.016 ± 0.14
IC 5309	-0.31 ± 0.22	1.48 ± 4.67	-0.087 ± 0.22	-0.18 ± 0.10	0.87 ± 2.85	-0.051 ± 0.12
NGC 1351	-0.17 ± 0.26	-0.73 ± 6.43	-0.043 ± 0.15	-0.06 ± 0.09	-0.27 ± 2.38	-0.016 ± 0.05
NGC 1366	-0.29 ± 0.24	4.58 ± 4.95	-0.038 ± 0.13	-0.71 ± 0.52	11.16 ± 12.97	-0.092 ± 0.31
NGC 1425	-0.07 ± 0.17	-1.73 ± 6.24	0.053 ± 0.18	-0.05 ± 0.13	-1.39 ± 4.91	0.042 ± 0.15
NGC 7515	-0.15 ± 0.18	0.40 ± 4.89	-0.040 ± 0.21	-0.10 ± 0.11	0.27 ± 3.38	-0.027 ± 0.14
NGC 7531	-0.21 ± 0.14	9.54 ± 3.93	0.029 ± 0.12	-0.40 ± 0.23	...	0.055 ± 0.24
NGC 7557	-0.31 ± 0.08	1.43 ± 3.90	0.164 ± 0.22	-0.60 ± 0.10	2.81 ± 8.85	0.321 ± 0.57
NGC 7631	0.02 ± 0.19	0.89 ± 5.82	0.324 ± 0.23	0.02 ± 0.26	1.22 ± 8.29	0.443 ± 0.43
NGC 7643	0.04 ± 0.11	0.19 ± 0.44	0.080 ± 0.17	0.06 ± 0.19	0.31 ± 0.79	0.133 ± 0.31

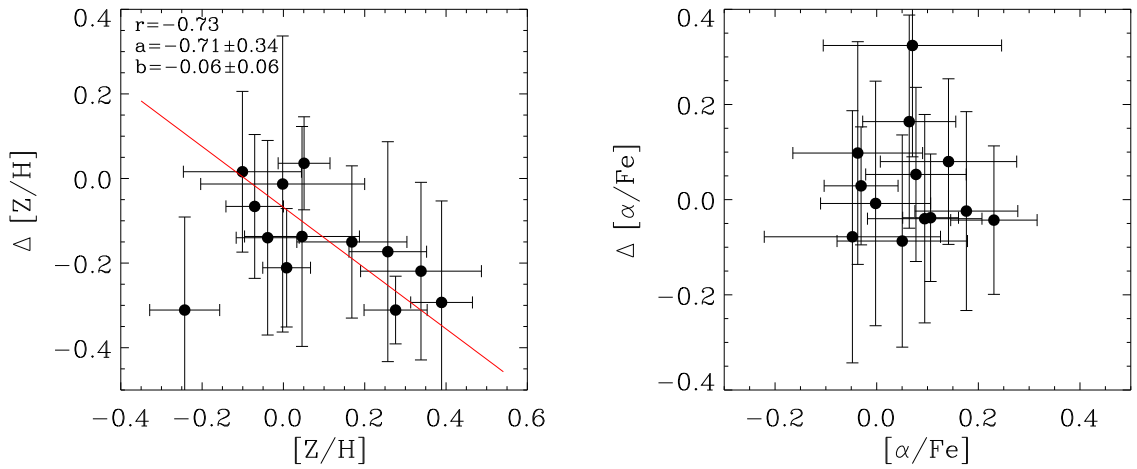

Figure 13. The gradient and central values of metallicity (left panel) and α/Fe enhancement (right panel). In the left panel the solid line represents the linear regression ($y = ax + b$) through all the data points. The Pearson correlation coefficient (r) and the results of the linear fit are given.

photometric, and kinematic properties, following the list of characteristics compiled by Kormendy & Kennicutt (2004). The more apply, the safer the classification becomes.

The apparent flattening of the bulge is similar to that of the disc in NGC 1292, NGC 1351 (Tab. 2). Moreover, most of the sample bulges have a Sérsic index $n \leqslant 2$. Only IC 5267, NGC 1351, NGC 1425, NGC 7515, and NGC 7631 have $n > 2$ (Tab. 2).

Pseudobulges are expected to be more rotation-dominated than classical bulges which are more rotation-dominated than giant elliptical galaxies (Kormendy & Kennicutt 2004). We measured the maximum rotation velocity $V_{\rm max}$ within $r_{\rm bd}$ from the stellar velocity curve and central velocity dispersion σ_0 from the velocity dispersion profile. The ellipticity ϵ of the bulge was measured by the photometric decomposition (Tab. 2). For each galaxy we derived the ratio $V_{\rm max}/\sigma_0$. In Fig. 14 we compared it to the value predicted for an oblate spheroid with isotropic velocity dispersion and the same observed ellipticity (Binney 1978, 1980; Binney & Tremaine 1987). The large error-bars on the $V_{\rm max}/\sigma_0$ are driven by uncertainties on the central velocity dispersion. Most of the sample bulges rotate as fast as both bulges of unbarred (Kormendy 1982, 1993; Kormendy & Illingworth 1982) and barred galaxies (Kormendy 1982; Aguerri et al. 2005). However, the values of $V_{\rm max}/\sigma_0$ measured for NGC 1292, NGC 1425, ESO 548-44, and NGC 5267 are significantly larger than that predicted for the oblate spheroids.

An other characteristic listed by Kormendy & Kennicutt (2004) is the position of pseudobulges with respect to the Faber-Jackson relation. The Faber-Jackson relation (FJ, Faber & Jackson 1976) relates the luminosity of the elliptical galaxies and early-type bulges to their central velocity dispersion. The pseudobulges

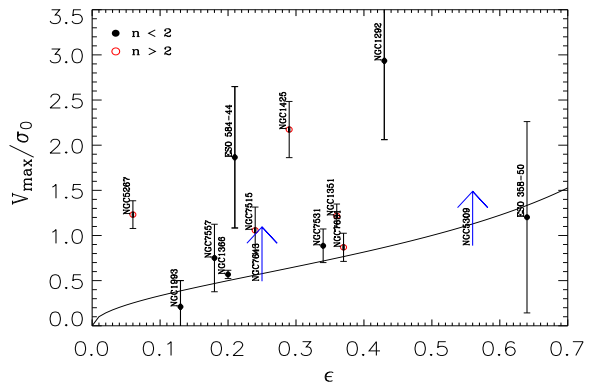

Figure 14. The location of the sample bulges in the $(V_{\rm max}/\sigma_0, \epsilon)$ plane. Filled and open circles correspond to bulges with Sérsic index $n \leqslant 2$ and $n > 2$, respectively. The continuous line corresponds to oblate-spheroidal systems that have isotropic velocity dispersions and that are flattened only by rotation.

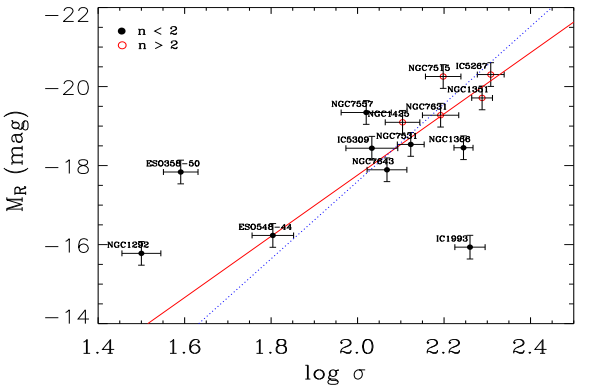

Figure 15. The location of the sample bulges with respect to the FJ relation by Forbes & Ponman (1999, blue dashed line). Filled and open circles correspond to bulges with Sérsic index $n \leqslant 2$ and $n > 2$, respectively and the linear fit is shown (red continuous line).

fall above the correlation (Kormendy & Kennicutt 2004). Sample bulges, except for ESO 358-G50 and NGC 1292, are consistent with the $R-$band FJ relation we built from Forbes & Ponman (1999, $L \propto \sigma^{3.92}$). They are characterized by a lower velocity dispersion or equivalently a higher luminosity with respect to their early-type counterparts (Fig. 15).

According to the prescriptions by Kormendy & Kennicutt (2004), the bulge of NGC 1292 is the most reliable pseudobulges in our sample. Information about its stellar population give more constraints on its nature and formation process. In fact, the bulge population has a intermediate age (3 Gyr) and low metal content ($[Z/{\rm H}] = -0.7$ dex). The $\alpha/{\rm Fe}$ enhancement is the lowest in our sample ($[\alpha/{\rm Fe}] = -0.12$ dex) suggesting a prolonged star formation history. The presence of emission lines in the spectrum shows that star formation is still ongoing. These properties are consistent with a slow buildup of the bulge of NGC 1292 within a scenario of secular evolution.

9 CONCLUSIONS

The structural parameters and properties of the stellar population of the bulges of sample of 14 S0 and spiral galaxies of the Fornax, Eridanus and Pegasus cluster, and NGC 7582 group were investigated to constrain the dominant mechanism at the epoch of their assembly.

- The bulge and disc parameters of the sample galaxies were derived performing a two-dimensional photometric decomposition of their $R-$band images. The surface-brightness distribution of the galaxy was assumed to be the sum of the contribution of a Sérsic bulge and an exponential disk. The two components were characterized by elliptical and concentric isophotes with constant (but possibly different) ellipticity and position angles. Most of the bulges have a Sérsic index $n \leqslant 2$ and for few of them the apparent flattening of the bulge is similar to that of the disc. According to Kormendy & Kennicutt (2004) the disc-like flattening and radial profile are the photometric signature of the pseudobulge.
- The central values of velocity dispersion σ and ${\rm Mg}_b$, ${\rm Mg}_2$, ${\rm H}_\beta$, $\langle{\rm Fe}\rangle$, and $[{\rm MgFe}]'$ line-strength indices were derived from the major-axis spectra. Correlations between ${\rm Mg}_2$, $\langle{\rm Fe}\rangle$, ${\rm H}_\beta$, and σ were found. The ${\rm Mg}_2-\sigma$ and ${\rm H}_\beta-\sigma$, correlations are steeper than those found for early-type galaxies (e.g., Bernardi et al. 1998; Jørgensen 1999a; Kuntschner 2000; Mehlert et al. 2003). The $\langle{\rm Fe}\rangle-\sigma$ correlation is consistent with previous findings for spiral bulges (Idiart et al. 1996; Prugniel et al. 2001; Proctor & Sansom 2002).
- The mean ages, total metallicities, and total $\alpha/{\rm Fe}$ enhancements in the center of the sample bulges were derived by using the stellar population models by Thomas et al. (2003). The youngest bulges have an average age of 2 Gyr. They are characterized by ongoing star formation. The stellar population of intermediate-age bulges is 4 to 8 Gyr old. It has solar metallicity ($[Z/{\rm H}] = 0.0$ dex). The older bulges have a narrow distribution in age around 10 Gyr and high metallicity ($[Z/{\rm H}] = 0.30$ dex). Most of the sample bulges display solar $\alpha/{\rm Fe}$ enhancements. A few have a central super-solar enhancement ($[\alpha/{\rm Fe}] = 0.3$).
- There is no correlation between age, metallicity, and $\alpha/{\rm Fe}$ enhancement of bulges with the membership of the host galaxy to different cluster. There is a correlation with the velocity dispersion. The more massive bulges of our sample galaxies are older, more metal rich and characterized by a fast star formation. Since we did not find any correlation with galaxy morphology we exclude a strong interplay between the bulge and disc components.
- Most of the sample galaxies show no gradient in age and a negative gradient of metallicity. This is in agreement with the earlier findings by Mehlert et al. (2003) and Sánchez-Blázquez et al. (2006) for the early-type galaxies, and by Jablonka et al. (2007) for bulges. The presence of negative gradient in the metallicity radial profile favors a scenario with bulge formation via dissipative collapse. This implies strong inside-out formation that should give rise to a negative gradient in the $\alpha/{\rm Fe}$ enhancement too (Ferreras & Silk 2002). But, no gradient was measured in the $[\alpha/{\rm Fe}]$ radial profiles for all the galaxies, except for NGC 1366 and NGC 7531. Moreover, the correlation between the central value and gradient of metallicity can not be built by pure dissipative collapse (Bekki & Shioya 1999; Kobayashi & Arimoto 1999) and suggests that mergers or acquisition events need to be invoked during the bulge assembly.
- The peculiar gradients observed for the stellar population of the bulges of NGC 1366 and NGC 7531 suggest they host a substructure. Very interestingly, in NGC 1366 we found the presence of

a kinematically-decoupled component. It is younger than the host bulge and formed by enriched material probably acquired via interaction or minor merging.

• According to the prescriptions by Kormendy & Kennicutt (2004) the bulge of NGC 1292 is a pseudobulge. The properties of its stellar population are consistent with a slow buildup within a scenario of secular evolution. Indeed, the bulge of NGC 1292 has a intermediate age (3 Gyr) and low metal content ($[Z/\mathrm{H}]= -0.7$ dex). The α/Fe enhancement is the lowest in our sample ($[\alpha/\mathrm{Fe}]= -0.12$ dex) suggesting a prolonged star formation history. The presence of emission lines in the spectrum is a signature of ongoing star formation.

ACKNOWLEDGMENTS

We thank David Burstein, Stephane Courteau, Reynier Peletier, and Alexandre Vazdekis for useful discussion and suggestions. LM is supported by grant (CPDR061795/06) by Padova University. University. FB, EMC, and AP receive support from grant PRIN2005/32 by Istituto Nazionale di Astrofisica (INAF) and from grant CPDA068415/06 by Padua University. LM and EMC acknowledge the Max-Planck-Institut fuer extraterrestrische Physik for hospitality while this paper was in progress.

REFERENCES

Afanasiev V. L., Sil'chenko O. K., 2005, A&A, 429, 825
Aguerri J. A. L., Balcells M., Peletier R. F., 2001, A&A, 367, 428
Aguerri J. A. L., Elias-Rosa N., Corsini E. M., Muñoz-Tuñón C., 2005, A&A, 434, 109
Aguerri J. A. L., Iglesias-Páramo J., Vílchez J. M., Muñoz-Tuñón C., Sánchez-Janssen R., 2005, AJ, 130, 475
Andredakis Y. C., Peletier R. F., Balcells M., 1995, MNRAS, 275, 874
Andredakis Y. C., Sanders R. H., 1994, MNRAS, 267, 283
Annibali F., Bressan A., Rampazzo R., Zeilinger W. W., Danese L., 2007, A&A, 463, 455
Arimoto N., Yoshii Y., 1987, A&A, 173, 23
Balcells M., Graham A. W., Domínguez-Palmero L., Peletier R. F., 2003, ApJL, 582, L79
Balogh M., Eke V., Miller C., Lewis I., Bower R., Couch W., Nichol R., Bland-Hawthorn J., Baldry I. K., Baugh C., Bridges T., Cannon R., Cole S., Colless M., Collins C., Cross N., Dalton G., 2004, MNRAS, 348, 1355
Bekki K., Shioya Y., 1999, ApJ, 513, 108
Bender R., Burstein D., Faber S. M., 1992, ApJ, 399, 462
Bender R., Burstein D., Faber S. M., 1993, ApJ, 411, 153
Berman S., 2001, A&A, 371, 476
Bernardi M., Renzini A., da Costa L. N., Wegner G., Alonso M. V., Pellegrini P. S., Rité C., Willmer C. N. A., 1998, ApJL, 508, L143
Bertola F., Corsini E. M., Vega Beltrán J. C., Pizzella A., Sarzi M., Cappellari M., Funes J. G., 1999, ApJL, 519, L127
Bertola F., Vietri M., Zeilinger W. W., 1991, ApJL, 374, L13
Bertola F., Zeilinger W. W., Rubin V. C., 1989, ApJL, 345, L29
Beuing J., Bender R., Mendes de Oliveira C., Thomas D., Maraston C., 2002, A&A, 395, 431
Binney J., 1978, MNRAS, 183, 501
Binney J., 1980, Royal Society of London Philosophical Transactions Series A, 296, 329
Binney J., Tremaine S., 1987, Galactic dynamics. Princeton, NJ, Princeton University Press, 1987, 747 p.
Brough S., Proctor R., Forbes D. A., Couch W. J., Collins C. A., Burke D. J., Mann R. G., 2007, MNRAS, 378, 1507
Bruzual G., Charlot S., 2003, MNRAS, 344, 1000
Burki G., Rufener F., Burnet M., Richard C., Blecha A., Bratschi P., 1995, A&AS, 112, 383
Burstein D., Bender R., Faber S., Nolthenius R., 1997, AJ, 114, 1365
Caon N., Capaccioli M., D'Onofrio M., 1993, MNRAS, 265, 1013
Cappellari M., Bacon R., Bureau M., Damen M. C., Davies R. L., de Zeeuw P. T., Emsellem E., Falcón-Barroso J., Krajnović D., Kuntschner H., McDermid R. M., Peletier R. F., Sarzi M., van den Bosch R. C. E., van de Ven G., 2006, MNRAS, 366, 1126
Carollo C. M., Stiavelli M., Mack J., 1998, AJ, 116, 68
Clemens M. S., Bressan A., Nikolic B., Alexander P., Annibali F., Rampazzo R., 2006, MNRAS, 370, 702
Coccato L., Corsini E. M., Pizzella A., Morelli L., Funes J. G., Bertola F., 2004, A&A, 416, 507
Cole S., Lacey C. G., Baugh C. M., Frenk C. S., 2000, MNRAS, 319, 168
Collobert M., Sarzi M., Davies R. L., Kuntschner H., Colless M., 2006, MNRAS, 370, 1213
Corsini E. M., Pizzella A., Coccato L., Bertola F., 2003, A&A, 408, 873
Corsini E. M., Pizzella A., Sarzi M., Cinzano P., Vega Beltrán J. C., Funes J. G., Bertola F., Persic M., Salucci P., 1999, A&A, 342, 671
Coziol R., Doyon R., Demers S., 2001, MNRAS, 325, 1081
Davies R. L., Illingworth G., 1983, ApJ, 266, 516
de Jong R. S., 1996, A&AS, 118, 557
de Vaucouleurs G., de Vaucouleurs A., Corwin H. G., Buta R. J., Paturel G., Fouque P., 1991, Third Reference Catalogue of Bright Galaxies. Volume 1-3, XII, 2069 pp. 7 figs.. Springer-Verlag Berlin Heidelberg New York
Denicoló G., Terlevich R., Terlevich E., Forbes D. A., Terlevich A., 2005, MNRAS, 358, 813
Dressler A., 1980, ApJ, 236, 351
Eggen O. J., Lynden-Bell D., Sandage A. R., 1962, ApJ, 136, 748
Emsellem E., Cappellari M., Peletier R. F., McDermid R. M., Bacon R., Bureau M., Copin Y., Davies R. L., Krajnović D., Kuntschner H., Miller B. W., Tim de Zeeuw P., 2004, MNRAS, 352, 721
Faber S. M., Jackson R. E., 1976, ApJ, 204, 668
Fathi K., Peletier R. F., 2003, A&A, 407, 61
Ferguson H. C., 1989, AJ, 98, 367
Ferreras I., Silk J., 2002, MNRAS, 336, 1181
Fisher D., Franx M., Illingworth G., 1996, ApJ, 459, 110
Forbes D. A., Ponman T. J., 1999, MNRAS, 309, 623
Fouque P., Gourgoulhon E., Chamaraux P., Paturel G., 1992, A&AS, 93, 211
Freeman K. C., 1970, ApJ, 160, 811
Ganda K., Peletier R. F., McDermid R. M., Falcón-Barroso J., de Zeeuw P. T., Bacon R., Cappellari M., Davies R. L., Emsellem E., Krajnović D., Kuntschner H., Sarzi M., van de Ven G., 2007, MNRAS, 380, 506
Garcia A. M., 1993, A&AS, 100, 47
Gerhard O. E., Vietri M., Kent S. M., 1989, ApJL, 345, L33
Gilmore G., Wyse R. F. G., 1998, AJ, 116, 748
Gorgas J., Efstathiou G., Salamanca A. A., 1990, MNRAS, 245, 217

Goudfrooij P., Gorgas J., Jablonka P., 1999, Astrophysics and Space Science, 269, 109
Graham A. W., 2001, MNRAS, 326, 543
Idiart T. P., de Freitas Pacheco J. A., Costa R. D. D., 1996, AJ, 112, 2541
Jablonka P., Gorgas J., Goudfrooij P., 2007, ArXiv e-prints, 707
Jablonka P., Martin P., Arimoto N., 1996, AJ, 112, 1415
Jørgensen I., 1999a, MNRAS, 306, 607
Jørgensen I., 1999b, MNRAS, 306, 607
Kauffmann G., 1996, MNRAS, 281, 487
Kobayashi C., Arimoto N., 1999, ApJ, 527, 573
Kodama T., Arimoto N., Barger A. J., Arag'on-Salamanca A., 1998, A&A, 334, 99
Kormendy J., 1977, ApJ, 217, 406
Kormendy J., 1982, ApJ, 257, 75
Kormendy J., 1993, in Dejonghe H., Habing H. J., eds, Galactic Bulges Vol. 153 of IAU Symposium, Kinematics of extragalactic bulges: evidence that some bulges are really disks. pp 209–+
Kormendy J., Gebhardt K., Macchetto F. D., Sparks W. B., 2001, AJ
Kormendy J., Illingworth G., 1982, ApJ, 256, 460
Kormendy J., Kennicutt R. C., 2004, ARA&A, 42, 603
Krajnović D., Jaffe W., 2004, A&A, 428, 877
Kuntschner H., 2000, MNRAS, 315, 184
Kuntschner H., Lucey J. R., Smith R. J., Hudson M. J., Davies R. L., 2001, MNRAS, 323, 615
Larson R. B., 1974, MNRAS, 166, 585
Lindblad B., 1956, Vistas in Astronomy, 2, 1711
MacArthur L. A., Courteau S., Holtzman J. A., 2003, ApJ, 582, 689
Matthews L. D., de Grijs R., 2004, AJ, 128, 137
McDermid R. M., Emsellem E., Shapiro K. L., Bacon R., Bureau M., Cappellari M., Davies R. L., de Zeeuw T., Falcón-Barroso J., Krajnović D., Kuntschner H., Peletier R. F., Sarzi M., 2006, MNRAS, 373, 906
Mehlert D., Saglia R. P., Bender R., Wegner G., 1998, A&A, 332, 33
Mehlert D., Saglia R. P., Bender R., Wegner G., 2000, A&AS, 141, 449
Mehlert D., Thomas D., Saglia R. P., Bender R., Wegner G., 2003, A&A, 407, 423
Mendez-Abreu J., Aguerri J. A. L., Corsini E. M., Simonneau E., 2007, ArXiv e-prints, 710
Möllenhoff C., Heidt J., 2001, A&A, 368, 16
Moore S. A. W., Lucey J. R., Kuntschner H., Colless M., 2002, MNRAS, 336, 382
Moorthy B. K., Holtzman J. A., 2006, MNRAS, 371, 583
Moré J. J., Garbow B. S., Hillstrom K. E., 1980, Argonne National Laboratory Report ANL-80-74
Morelli L., Halliday C., Corsini E. M., Pizzella A., Thomas D., Saglia R. P., Davies R. L., Bender R., Birkinshaw M., Bertola F., 2004, MNRAS, 354, 753
Nishiura S., Shimada M., Ohyama Y., Murayama T., Taniguchi Y., 2000, AJ, 120, 1691
Osterbrock D. E., Fulbright J. P., Martel A. R., Keane M. J., Trager S. C., Basri G., 1996, PASP, 108, 277
Paturel G., Petit C., Prugniel P., Theureau G., Rousseau J., Brouty M., Dubois P., Cambrésy L., 2003, A&A, 412, 45
Peletier R. F., 1989, PhD thesis, University of Groningen
Peletier R. F., Falcón-Barroso J., Bacon R., Cappellari M., Davies R. L., de Zeeuw P. T., Emsellem E., Ganda K., Krajnović D., Kuntschner H., McDermid R. M., Sarzi M., van de Ven G., 2007, MNRAS, 379, 445
Pizzella A., Corsini E. M., Morelli L., Sarzi M., Scarlata C., Stiavelli M., Bertola F., 2002, ApJ, 573, 131
Proctor R. N., Sansom A. E., 2002, MNRAS, 333, 517
Prugniel P., Maubon G., Simien F., 2001, A&A, 366, 68
Rampazzo R., Annibali F., Bressan A., Longhetti M., Padoan F., Zeilinger W. W., 2005, A&A, 433, 497
Reda F. M., Proctor R. N., Forbes D. A., Hau G. K. T., Larsen S. S., 2007, MNRAS, 377, 1772
Salpeter E. E., 1955, ApJ, 121, 161
Sánchez-Blázquez P., Gorgas J., Cardiel N., 2006, A&A, 457, 823
Sánchez-Blázquez P., Gorgas J., Cardiel N., González J. J., 2006, A&A, 457, 809
Sandage A., 1990, JARSC, 84, 70
Sarzi M., Corsini E. M., Pizzella A., Vega Beltrán J. C., Cappellari M., Funes J. G., Bertola F., 2000, A&A, 360, 439
Sarzi M., Falcón-Barroso J., Davies R. L., Bacon R., Bureau M., Cappellari M., de Zeeuw P. T., Emsellem E., Fathi K., Krajnović D., Kuntschner H., McDermid R. M., Peletier R. F., 2006, MNRAS, 366, 1151
Sersic J. L., 1968, Atlas de galaxias australes. Cordoba, Argentina: Observatorio Astronomico, 1968
Thomas D., Davies R. L., 2006, MNRAS, 366, 510
Thomas D., Maraston C., Bender R., 2003, MNRAS, 339, 897
Thomas D., Maraston C., Bender R., Mendes de Oliveira C., 2005, ApJ, 621, 673
Tinsley B. M., 1980, Fundamentals of Cosmic Physics, 5, 287
Trager S. C., Dalcanton J. J., Weiner B. J., 1999, in The Formation of Galactic Bulges Integrated Stellar Populations of Bulges: First Results. pp 42–+
Trager S. C., Faber S. M., Worthey G., González J. J., 2000, AJ, 119, 1645
Trager S. C., Worthey G., Faber S. M., Burstein D., Gonzalez J. J., 1998, ApJS, 116, 1
Tremonti C. A., Heckman T. M., Kauffmann G., Brinchmann J., Charlot S., White S. D. M., Seibert M., Peng E. W., Schlegel D. J., Uomoto A., Fukugita M., Brinkmann J., 2004, ApJ, 613, 898
Worthey G., Faber S. M., Gonzalez J. J., 1992, ApJ, 398, 69
Worthey G., Faber S. M., Gonzalez J. J., Burstein D., 1994, ApJS, 94, 687
Zaritsky D., Lo K. Y., 1986, ApJ, 303, 66

APPENDIX A: KINEMATICS RESULTS

Figure A1. Kinematic parameters measured along the major axis of the galaxies. For each galaxy the curve is folded around the nucleus. Asterisks and dots refer to the two sides (est/west) of the galaxy. The radial profiles of the line-of-sight velocity (v) after the subtraction of the systemic velocity and velocity dispersion (σ) are shown from top to bottom. For NGC 1292, IC 1993, ESO 358-50 and ESO 548-44, only the central value of σ was measured and it is tabulated in Tab. 3. The vertical dashed line indicates the radius ($r_{\rm db}$) where the surface-brightness contributions of bulge and disc are the same.

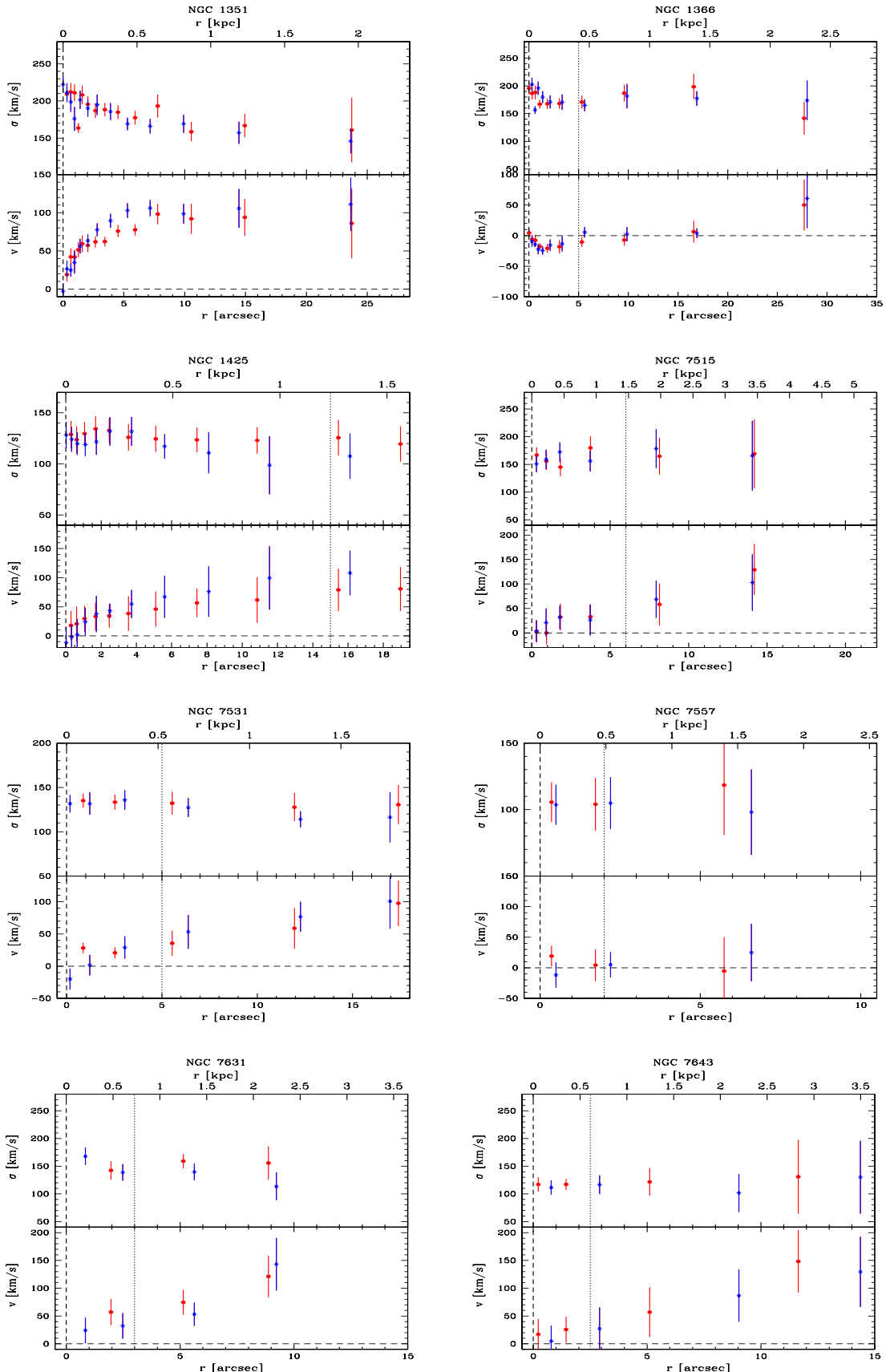

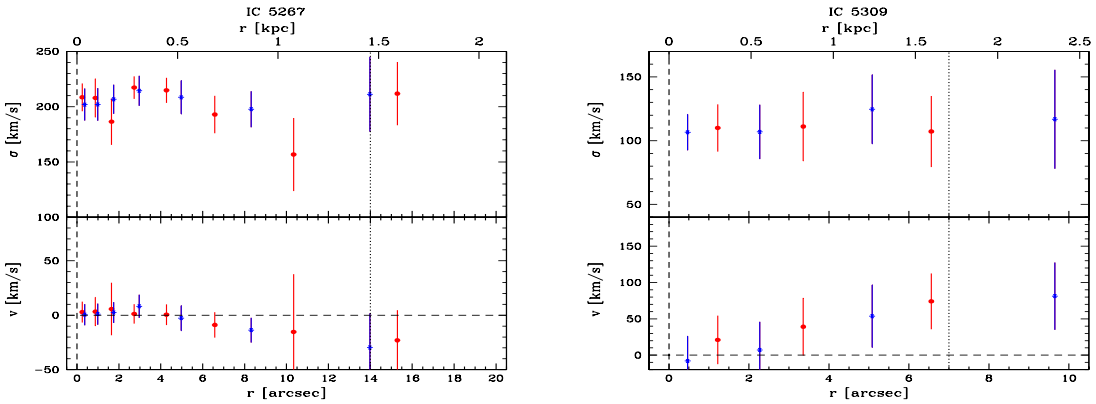

Figure A1 – *continued*

APPENDIX B: STELLAR KINEMATIC AND LINE STRENGTH INDICES.

This paper has been typeset from a TEX/ LATEX file prepared by the author.

Table B1. Stellar kinematic and line strength indices of the sample galaxies.The columns show the following: (1) radius along the major axis, (2) rotation velocity, subtracted of the galaxy systemic velocity, along the major axis, (3) rotation velocity dispersion, (4), (5), (6), (7), (8) measured values for Mg_2, Mg_b, Fe5270, Fe5335, H_β respectively. Positive and negative values are respectively for absorption and emission line strength.Column (9) shows the applied correction to H_β absorption index.

r (arcsec) (1)	V ($\mathrm{km\ s^{-1}}$) (2)	σ ($\mathrm{km\ s^{-1}}$) (3)	Mg_2 (mag) (4)	Mg_b (Å) (5)	Fe5270 (Å) (6)	Fe5335 (Å) (7)	H_β (Å) (8)	$\Delta\,\mathrm{H}_\beta$ (Å) (9)
ESO 358-50								
-10.9	-25.1 ± 43.1	...	0.149 ± 0.017	2.826 ± 0.683	2.337 ± 0.816	2.304 ± 0.996	2.35 ± 0.59	0.00
-6.1	-21.9 ± 36.3	...	0.163 ± 0.008	2.641 ± 0.341	2.422 ± 0.408	2.199 ± 0.506	1.99 ± 0.29	0.00
-1.6	-5.5 ± 31.4	...	0.157 ± 0.007	2.822 ± 0.270	2.587 ± 0.327	2.297 ± 0.400	2.34 ± 0.23	0.00
1.4	10.0 ± 18.1	...	0.154 ± 0.003	2.669 ± 0.135	2.491 ± 0.157	2.412 ± 0.189	2.35 ± 0.11	0.00
5.2	10.1 ± 38.5	...	0.152 ± 0.008	2.645 ± 0.324	2.643 ± 0.378	2.419 ± 0.462	2.37 ± 0.27	0.00
9.9	32.4 ± 41.8	...	0.156 ± 0.012	2.841 ± 0.506	2.572 ± 0.606	2.235 ± 0.768	2.20 ± 0.41	0.00
ESO 548-44								
-8.7	35.0 ± 36.8	...	0.137 ± 0.013	2.262 ± 0.406	2.269 ± 0.484	2.635 ± 0.591	1.78 ± 0.35	0.00
-3.5	20.9 ± 36.1	...	0.174 ± 0.013	2.774 ± 0.415	2.788 ± 0.502	2.333 ± 0.614	1.58 ± 0.37	0.00
-0.8	7.9 ± 43.7	...	0.194 ± 0.013	3.139 ± 0.409	2.994 ± 0.490	2.644 ± 0.577	1.77 ± 0.36	0.00
0.3	0.1 ± 48.1	...	0.190 ± 0.012	3.045 ± 0.399	2.861 ± 0.476	2.557 ± 0.558	2.01 ± 0.35	0.00
2.3	33.7 ± 51.0	...	0.179 ± 0.012	2.719 ± 0.392	2.789 ± 0.455	2.295 ± 0.552	1.71 ± 0.33	0.00
7.3	30.5 ± 38.4	...	0.150 ± 0.012	2.615 ± 0.405	2.363 ± 0.480	2.335 ± 0.584	2.04 ± 0.34	0.00
IC 1993								
-9.6	-15.0 ± 45.2	...	0.143 ± 0.017	2.569 ± 0.503	2.222 ± 0.597	1.776 ± 0.696	1.76 ± 0.44	0.00
-4.6	-10.2 ± 49.5	...	0.165 ± 0.013	2.955 ± 0.407	2.419 ± 0.478	2.155 ± 0.557	2.08 ± 0.35	0.00
-1.1	5.8 ± 38.2	...	0.184 ± 0.007	3.084 ± 0.198	2.617 ± 0.235	2.268 ± 0.275	2.12 ± 0.17	0.00
0.6	19.0 ± 40.3	...	0.176 ± 0.008	3.070 ± 0.234	2.955 ± 0.276	2.464 ± 0.332	2.05 ± 0.20	0.00
3.7	12.1 ± 44.7	...	0.162 ± 0.017	2.892 ± 0.515	2.853 ± 0.610	2.423 ± 0.714	2.13 ± 0.45	0.00
8.9	-11.5 ± 63.1	...	0.152 ± 0.038	2.595 ± 1.150	2.291 ± 1.365	1.606 ± 1.605	1.74 ± 1.01	0.00
IC 5267								
-13.9	29.5 ± 31.3	211.2 ± 33.8	0.233 ± 0.013	3.849 ± 0.515	2.779 ± 0.481	2.501 ± 0.619	1.73 ± 0.33	0.04
-8.3	13.6 ± 11.3	197.7 ± 16.3	0.242 ± 0.007	4.025 ± 0.273	2.891 ± 0.258	2.714 ± 0.334	1.73 ± 0.17	0.01
-4.9	2.6 ± 11.5	208.5 ± 15.1	0.256 ± 0.007	4.333 ± 0.255	3.178 ± 0.240	2.715 ± 0.315	1.14 ± 0.16	0.55
-2.9	-8.2 ± 10.6	214.4 ± 13.6	0.262 ± 0.006	4.299 ± 0.245	3.148 ± 0.230	2.840 ± 0.303	0.99 ± 0.16	0.85
-1.7	-2.5 ± 9.5	206.7 ± 13.1	0.284 ± 0.006	4.678 ± 0.236	3.112 ± 0.222	2.797 ± 0.291	1.07 ± 0.15	0.85
-0.9	-1.0 ± 9.7	202.0 ± 14.7	0.283 ± 0.006	4.617 ± 0.237	3.231 ± 0.223	3.097 ± 0.290	1.13 ± 0.15	0.70
-0.3	-0.5 ± 9.7	201.9 ± 14.5	0.283 ± 0.006	4.660 ± 0.237	3.182 ± 0.223	2.949 ± 0.290	1.07 ± 0.15	0.47
0.2	2.8 ± 9.6	208.5 ± 12.6	0.282 ± 0.006	4.743 ± 0.236	3.310 ± 0.221	3.014 ± 0.290	1.11 ± 0.15	0.36
0.8	3.2 ± 13.2	207.9 ± 17.4	0.280 ± 0.008	4.728 ± 0.309	3.049 ± 0.291	2.926 ± 0.380	1.06 ± 0.20	0.06
1.6	5.6 ± 24.1	186.4 ± 20.9	0.269 ± 0.010	4.363 ± 0.366	3.055 ± 0.344	2.726 ± 0.443	1.08 ± 0.24	0.43
2.7	1.1 ± 8.9	217.3 ± 10.2	0.260 ± 0.005	4.408 ± 0.210	2.965 ± 0.198	2.782 ± 0.262	1.18 ± 0.13	0.43
4.2	0.4 ± 9.5	214.8 ± 11.3	0.250 ± 0.006	4.200 ± 0.230	2.974 ± 0.217	2.764 ± 0.286	1.31 ± 0.15	0.46
6.5	-8.9 ± 11.7	192.9 ± 16.9	0.245 ± 0.007	3.900 ± 0.276	2.875 ± 0.260	2.592 ± 0.336	1.52 ± 0.18	0.01
10.3	-15.3 ± 53.0	156.7 ± 33.1	0.239 ± 0.009	3.881 ± 0.342	2.691 ± 0.328	2.424 ± 0.407	1.59 ± 0.23	0.08
15.2	-23.0 ± 27.6	211.8 ± 28.6	0.229 ± 0.013	3.922 ± 0.480	3.133 ± 0.458	2.622 ± 0.596	1.48 ± 0.31	0.02
IC 5309								
-6.5	74.1 ± 38.4	107.2 ± 27.9	0.125 ± 0.010	2.225 ± 0.363	1.811 ± 0.431	1.315 ± 0.508	0.09 ± 0.32	2.72
-3.3	39.1 ± 39.5	111.1 ± 27.1	0.130 ± 0.010	1.884 ± 0.362	2.233 ± 0.432	2.012 ± 0.529	-1.63 ± 0.33	3.99
-1.2	21.0 ± 33.5	110.0 ± 18.5	0.124 ± 0.006	2.053 ± 0.242	2.038 ± 0.288	1.984 ± 0.347	-0.46 ± 0.21	2.99
0.4	7.9 ± 34.0	106.6 ± 14.1	0.135 ± 0.004	2.445 ± 0.164	2.061 ± 0.197	1.971 ± 0.237	0.45 ± 0.14	2.23
2.2	-7.1 ± 38.7	106.9 ± 21.3	0.126 ± 0.007	2.262 ± 0.274	1.996 ± 0.324	1.913 ± 0.388	-0.26 ± 0.24	2.74
5.0	-53.6 ± 43.0	124.6 ± 27.1	0.121 ± 0.010	1.851 ± 0.363	1.975 ± 0.433	1.271 ± 0.539	-0.93 ± 0.32	3.62
9.6	-81.2 ± 46.3	116.8 ± 38.8	0.115 ± 0.018	2.185 ± 0.692	2.169 ± 0.819	1.402 ± 1.013	-0.05 ± 0.61	2.72

Table B1 – *continued*

(1)	(2)	(3)	(4)	(5)	(6)	(7)	(8)	(9)
NGC 1292								
-11.2	-41.4 ± 24.5	...	0.085 ± 0.011	1.836 ± 0.456	1.888 ± 0.541	1.568 ± 0.635	-0.79 ± 0.40	3.70
-5.4	-28.7 ± 25.3	...	0.097 ± 0.011	1.824 ± 0.464	1.519 ± 0.560	1.408 ± 0.653	-0.53 ± 0.42	3.16
-1.6	0.1 ± 23.3	...	0.101 ± 0.011	1.734 ± 0.447	2.019 ± 0.540	1.313 ± 0.655	-0.80 ± 0.41	3.74
1.2	10.3 ± 23.9	...	0.103 ± 0.011	1.607 ± 0.461	1.853 ± 0.550	1.416 ± 0.673	-0.29 ± 0.41	3.01
4.5	29.0 ± 23.6	...	0.101 ± 0.011	2.009 ± 0.460	1.911 ± 0.533	1.617 ± 0.664	0.09 ± 0.40	2.82
9.8	30.4 ± 25.7	...	0.095 ± 0.012	1.922 ± 0.478	1.712 ± 0.554	1.482 ± 0.689	-1.45 ± 0.43	3.57
NGC 1351								
-23.7	86.0 ± 45.4	160.9 ± 43.1	0.183 ± 0.012	3.111 ± 0.416	1.754 ± 0.490	2.012 ± 0.626	1.79 ± 0.35	0.00
-14.9	93.9 ± 24.0	166.8 ± 15.3	0.201 ± 0.008	3.531 ± 0.273	2.374 ± 0.326	2.043 ± 0.410	1.73 ± 0.22	0.00
-10.5	92.0 ± 19.5	158.5 ± 12.8	0.202 ± 0.005	3.707 ± 0.168	2.498 ± 0.200	1.892 ± 0.251	1.60 ± 0.14	0.00
-7.7	98.2 ± 13.2	193.2 ± 15.6	0.214 ± 0.007	4.034 ± 0.262	2.581 ± 0.315	2.485 ± 0.402	1.68 ± 0.21	0.00
-5.9	77.6 ± 7.4	177.5 ± 9.2	0.231 ± 0.004	4.182 ± 0.149	2.377 ± 0.174	2.228 ± 0.226	1.85 ± 0.12	0.00
-4.5	75.9 ± 7.7	184.9 ± 9.2	0.241 ± 0.004	3.987 ± 0.163	2.454 ± 0.190	2.479 ± 0.248	1.80 ± 0.13	0.00
-3.4	62.3 ± 6.4	188.3 ± 9.0	0.254 ± 0.004	4.396 ± 0.155	2.736 ± 0.184	2.580 ± 0.236	1.63 ± 0.13	0.00
-2.6	61.9 ± 7.3	187.0 ± 9.9	0.260 ± 0.005	4.164 ± 0.166	2.848 ± 0.197	2.828 ± 0.253	1.61 ± 0.14	0.00
-2.0	57.2 ± 8.7	195.5 ± 11.1	0.276 ± 0.005	4.560 ± 0.185	3.000 ± 0.219	2.435 ± 0.284	1.63 ± 0.15	0.00
-1.5	59.3 ± 11.1	208.2 ± 12.6	0.286 ± 0.006	4.879 ± 0.207	3.196 ± 0.245	2.955 ± 0.320	1.73 ± 0.17	0.00
-1.2	51.5 ± 9.8	163.6 ± 6.6	0.293 ± 0.002	4.679 ± 0.068	2.913 ± 0.080	3.095 ± 0.101	1.55 ± 0.05	0.00
-0.9	41.9 ± 9.8	211.0 ± 11.4	0.292 ± 0.005	4.958 ± 0.182	2.879 ± 0.219	2.865 ± 0.283	1.73 ± 0.15	0.00
-0.6	42.2 ± 10.5	212.3 ± 12.0	0.300 ± 0.005	5.114 ± 0.193	3.209 ± 0.231	2.850 ± 0.301	1.72 ± 0.15	0.00
-0.3	19.0 ± 8.9	209.3 ± 10.6	0.302 ± 0.005	5.197 ± 0.167	3.084 ± 0.200	2.890 ± 0.250	1.45 ± 0.13	0.00
0.0	-2.7 ± 10.7	222.3 ± 10.6	0.297 ± 0.005	5.001 ± 0.203	3.409 ± 0.243	2.942 ± 0.310	1.55 ± 0.16	0.00
0.3	-26.5 ± 10.8	211.5 ± 12.5	0.297 ± 0.005	4.775 ± 0.201	2.827 ± 0.234	2.745 ± 0.313	1.50 ± 0.16	0.00
0.6	-24.9 ± 8.5	198.7 ± 13.3	0.280 ± 0.005	4.790 ± 0.191	2.933 ± 0.222	2.799 ± 0.293	1.69 ± 0.15	0.00
0.9	-34.9 ± 14.6	176.1 ± 16.2	0.282 ± 0.005	4.671 ± 0.189	2.679 ± 0.224	2.576 ± 0.285	1.46 ± 0.16	0.00
1.4	-56.2 ± 9.5	201.6 ± 12.4	0.274 ± 0.005	4.632 ± 0.182	2.868 ± 0.218	2.670 ± 0.280	1.69 ± 0.15	0.00
2.0	-63.3 ± 8.1	190.2 ± 11.4	0.259 ± 0.005	4.227 ± 0.190	2.745 ± 0.227	2.722 ± 0.289	1.60 ± 0.15	0.00
2.8	-77.6 ± 8.5	194.9 ± 13.8	0.252 ± 0.005	4.311 ± 0.195	2.857 ± 0.234	2.449 ± 0.285	1.66 ± 0.16	0.00
3.8	-89.4 ± 9.2	185.8 ± 11.4	0.238 ± 0.005	4.142 ± 0.194	3.026 ± 0.232	2.354 ± 0.286	1.59 ± 0.16	0.00
5.2	-102.9 ± 9.6	169.3 ± 8.4	0.224 ± 0.004	4.022 ± 0.152	2.652 ± 0.181	2.619 ± 0.220	1.73 ± 0.12	0.00
7.1	-106.1 ± 10.5	166.1 ± 9.6	0.210 ± 0.004	3.770 ± 0.161	2.597 ± 0.193	2.454 ± 0.233	1.61 ± 0.13	0.00
9.9	-98.5 ± 13.0	169.3 ± 12.2	0.200 ± 0.006	3.351 ± 0.203	2.299 ± 0.244	1.898 ± 0.297	1.42 ± 0.17	0.00
14.4	-105.7 ± 25.1	157.2 ± 14.6	0.193 ± 0.006	3.275 ± 0.209	2.098 ± 0.251	1.860 ± 0.302	1.46 ± 0.17	0.00
23.6	-111.0 ± 34.7	145.8 ± 16.1	0.179 ± 0.007	3.151 ± 0.258	2.142 ± 0.307	2.078 ± 0.377	0.96 ± 0.22	0.00
NGC 1366								
-27.6	50.1 ± 41.3	141.6 ± 29.4	0.175 ± 0.014	2.588 ± 0.492	2.320 ± 0.566	1.487 ± 0.728	1.50 ± 0.42	0.00
-16.5	6.4 ± 17.6	198.4 ± 22.2	0.183 ± 0.011	2.862 ± 0.407	2.380 ± 0.490	2.354 ± 0.627	1.69 ± 0.33	0.00
-9.5	-7.0 ± 10.0	186.9 ± 15.0	0.200 ± 0.007	3.338 ± 0.267	2.657 ± 0.319	2.248 ± 0.394	1.81 ± 0.22	0.00
-5.3	-10.4 ± 7.7	170.8 ± 11.4	0.204 ± 0.006	3.332 ± 0.214	2.852 ± 0.254	2.677 ± 0.309	1.81 ± 0.17	0.00
-3.0	-18.1 ± 10.5	168.2 ± 9.2	0.216 ± 0.005	3.754 ± 0.191	2.924 ± 0.227	2.647 ± 0.276	1.68 ± 0.15	0.00
-1.8	-20.7 ± 7.4	167.6 ± 9.1	0.235 ± 0.005	3.875 ± 0.185	3.076 ± 0.219	2.721 ± 0.267	1.89 ± 0.15	0.00
-1.0	-17.7 ± 5.8	167.0 ± 8.1	0.249 ± 0.004	4.135 ± 0.162	3.184 ± 0.191	2.674 ± 0.232	2.02 ± 0.13	0.00
-0.6	-7.5 ± 9.0	188.3 ± 12.5	0.258 ± 0.006	3.979 ± 0.214	3.325 ± 0.254	2.971 ± 0.313	1.87 ± 0.17	0.00
-0.3	-6.1 ± 7.7	186.6 ± 11.1	0.267 ± 0.005	4.402 ± 0.195	3.404 ± 0.231	3.129 ± 0.284	1.65 ± 0.16	0.00
-0.0	4.5 ± 8.0	195.7 ± 11.3	0.264 ± 0.005	4.326 ± 0.193	3.265 ± 0.229	3.070 ± 0.293	1.99 ± 0.15	0.00
0.3	9.4 ± 9.0	202.7 ± 11.9	0.261 ± 0.006	4.205 ± 0.208	3.532 ± 0.246	3.143 ± 0.318	1.90 ± 0.16	0.00
0.6	14.3 ± 4.2	156.6 ± 6.6	0.263 ± 0.002	4.218 ± 0.054	3.107 ± 0.063	2.937 ± 0.079	1.71 ± 0.04	0.00
0.9	22.3 ± 8.3	195.9 ± 11.9	0.257 ± 0.005	4.255 ± 0.202	3.207 ± 0.237	3.077 ± 0.307	1.71 ± 0.16	0.00
1.3	24.3 ± 6.7	179.7 ± 10.8	0.249 ± 0.005	4.087 ± 0.189	3.208 ± 0.221	2.950 ± 0.283	1.82 ± 0.15	0.00
2.1	15.6 ± 9.3	171.1 ± 11.7	0.238 ± 0.006	3.814 ± 0.217	2.940 ± 0.257	2.758 ± 0.324	1.79 ± 0.18	0.00
3.3	13.3 ± 12.4	170.7 ± 14.0	0.221 ± 0.006	3.689 ± 0.231	2.870 ± 0.274	2.879 ± 0.343	1.50 ± 0.19	0.00
5.6	-5.4 ± 8.3	164.9 ± 10.5	0.207 ± 0.006	3.572 ± 0.230	2.602 ± 0.274	2.393 ± 0.332	1.41 ± 0.19	0.00
9.8	-2.4 ± 11.6	181.6 ± 22.1	0.199 ± 0.008	3.475 ± 0.294	2.345 ± 0.352	2.401 ± 0.434	1.69 ± 0.24	0.00
16.8	-3.9 ± 7.9	177.2 ± 13.2	0.192 ± 0.006	3.306 ± 0.222	2.462 ± 0.265	2.136 ± 0.328	1.68 ± 0.18	0.00
27.9	-60.8 ± 48.5	173.8 ± 35.8	0.180 ± 0.015	3.244 ± 0.535	1.961 ± 0.639	2.288 ± 0.810	1.09 ± 0.45	0.00

Table B1 – *continued*

(1)	(2)	(3)	(4)	(5)	(6)	(7)	(8)	(9)
NGC 1425								
−18.9	80.8 ± 37.5	119.6 ± 17.2	0.162 ± 0.008	2.864 ± 0.338	2.108 ± 0.403	1.332 ± 0.495	2.55 ± 0.28	0.00
−15.4	79.1 ± 36.4	125.6 ± 17.5	0.170 ± 0.008	2.809 ± 0.318	2.410 ± 0.378	2.233 ± 0.461	2.00 ± 0.27	0.00
−10.8	61.8 ± 39.1	123.0 ± 12.7	0.169 ± 0.005	2.923 ± 0.201	2.151 ± 0.240	2.376 ± 0.289	2.20 ± 0.17	0.00
−7.4	56.8 ± 24.2	123.5 ± 11.8	0.175 ± 0.004	3.248 ± 0.154	2.392 ± 0.185	2.299 ± 0.224	1.98 ± 0.13	0.00
−5.1	46.1 ± 29.8	124.5 ± 12.7	0.191 ± 0.004	3.298 ± 0.175	2.451 ± 0.205	2.089 ± 0.249	1.98 ± 0.15	0.00
−3.5	38.5 ± 29.8	126.0 ± 13.0	0.196 ± 0.004	3.242 ± 0.176	2.530 ± 0.210	2.278 ± 0.255	1.51 ± 0.15	0.00
−2.4	34.3 ± 19.6	132.8 ± 12.0	0.204 ± 0.004	3.376 ± 0.146	2.840 ± 0.174	2.297 ± 0.213	1.72 ± 0.13	0.00
−1.6	33.4 ± 23.6	134.3 ± 12.3	0.212 ± 0.004	3.516 ± 0.163	2.571 ± 0.195	2.364 ± 0.239	1.73 ± 0.14	0.00
−1.0	29.6 ± 22.4	129.7 ± 11.2	0.224 ± 0.004	3.461 ± 0.144	2.796 ± 0.174	2.300 ± 0.210	1.87 ± 0.12	0.00
−0.6	20.8 ± 29.9	123.7 ± 13.1	0.227 ± 0.004	3.534 ± 0.173	2.853 ± 0.209	2.456 ± 0.250	1.74 ± 0.15	0.00
−0.2	18.1 ± 24.8	128.9 ± 13.3	0.228 ± 0.004	3.671 ± 0.163	2.977 ± 0.198	2.709 ± 0.245	1.81 ± 0.14	0.00
0.0	11.7 ± 25.7	128.3 ± 12.9	0.229 ± 0.004	3.763 ± 0.171	3.005 ± 0.203	2.543 ± 0.252	1.64 ± 0.15	0.00
0.3	2.1 ± 21.7	124.0 ± 12.0	0.224 ± 0.004	3.636 ± 0.153	2.961 ± 0.182	2.583 ± 0.225	1.79 ± 0.13	0.00
0.6	1.9 ± 26.9	119.8 ± 10.9	0.218 ± 0.004	3.702 ± 0.142	2.931 ± 0.167	2.536 ± 0.206	1.77 ± 0.12	0.00
1.0	24.1 ± 23.9	118.9 ± 10.9	0.212 ± 0.004	3.625 ± 0.148	2.857 ± 0.176	2.461 ± 0.215	1.60 ± 0.12	0.00
1.7	37.8 ± 31.2	121.6 ± 12.7	0.205 ± 0.004	3.529 ± 0.173	2.556 ± 0.207	2.199 ± 0.245	1.67 ± 0.15	0.00
2.5	43.1 ± 12.3	131.9 ± 13.9	0.199 ± 0.004	3.390 ± 0.180	2.361 ± 0.216	2.335 ± 0.263	1.74 ± 0.15	0.00
3.7	54.8 ± 24.2	131.8 ± 14.1	0.195 ± 0.004	3.243 ± 0.180	2.647 ± 0.209	2.208 ± 0.256	1.67 ± 0.15	0.00
5.6	67.1 ± 36.2	117.2 ± 11.9	0.184 ± 0.004	3.041 ± 0.152	2.437 ± 0.180	2.091 ± 0.218	1.75 ± 0.13	0.00
8.1	76.2 ± 43.3	110.8 ± 19.9	0.187 ± 0.007	3.150 ± 0.274	2.382 ± 0.331	2.028 ± 0.393	1.87 ± 0.24	0.00
11.5	99.5 ± 54.4	98.7 ± 28.4	0.172 ± 0.012	2.807 ± 0.471	2.471 ± 0.555	2.064 ± 0.677	2.05 ± 0.40	0.00
16.1	108.0 ± 38.3	107.6 ± 22.1	0.163 ± 0.006	2.748 ± 0.241	2.433 ± 0.282	1.981 ± 0.346	2.08 ± 0.20	0.00
NGC 7515								
−14.188	129.0 ± 51.4	169.0 ± 61.9	0.126 ± 0.023	2.325 ± 0.917	2.284 ± 1.013	2.231 ± 1.270	−1.61 ± 0.74	5.08
−8.137	58.3 ± 42.8	164.6 ± 33.6	0.171 ± 0.015	3.182 ± 0.596	2.275 ± 0.639	2.124 ± 0.827	0.35 ± 0.47	1.67
−3.742	33.0 ± 23.3	179.7 ± 20.7	0.189 ± 0.008	2.982 ± 0.311	2.784 ± 0.339	2.541 ± 0.435	1.79 ± 0.23	0.26
−1.821	32.5 ± 26.8	145.0 ± 15.8	0.205 ± 0.005	3.459 ± 0.201	2.842 ± 0.218	2.497 ± 0.274	1.80 ± 0.15	0.32
−0.933	−0.1 ± 22.8	155.8 ± 15.4	0.214 ± 0.005	3.649 ± 0.215	2.778 ± 0.237	2.714 ± 0.285	2.12 ± 0.16	0.21
−0.314	2.4 ± 21.8	166.8 ± 13.7	0.220 ± 0.005	3.591 ± 0.201	2.954 ± 0.221	2.883 ± 0.269	1.99 ± 0.15	0.00
0.292	−4.0 ± 21.9	150.8 ± 14.9	0.216 ± 0.005	3.676 ± 0.202	2.849 ± 0.222	2.494 ± 0.268	2.03 ± 0.15	0.07
0.909	−21.1 ± 29.0	158.8 ± 17.7	0.207 ± 0.007	3.634 ± 0.287	2.872 ± 0.315	2.804 ± 0.393	1.98 ± 0.22	0.10
1.794	−31.9 ± 23.8	172.2 ± 17.4	0.188 ± 0.007	3.324 ± 0.260	2.754 ± 0.286	2.346 ± 0.363	1.92 ± 0.20	0.02
3.719	−26.5 ± 31.5	156.0 ± 18.3	0.192 ± 0.008	3.279 ± 0.323	2.741 ± 0.355	2.381 ± 0.445	1.79 ± 0.25	0.00
7.926	−68.7 ± 37.8	178.3 ± 35.0	0.178 ± 0.015	3.335 ± 0.602	2.489 ± 0.657	2.348 ± 0.843	1.48 ± 0.46	0.86
14.060	−102.9 ± 57.4	165.8 ± 62.6	0.136 ± 0.024	2.045 ± 0.960	2.076 ± 1.060	1.193 ± 1.301	0.91 ± 0.75	2.06
NGC 7531								
−17.3	97.6 ± 35.5	130.5 ± 22.2	0.204 ± 0.009	3.792 ± 0.355	1.497 ± 0.401	1.764 ± 0.477	1.83 ± 0.28	0.04
−11.9	58.8 ± 31.5	127.7 ± 15.6	0.182 ± 0.006	3.193 ± 0.198	2.589 ± 0.215	2.448 ± 0.272	2.01 ± 0.15	0.03
−5.5	35.5 ± 19.4	132.2 ± 13.0	0.200 ± 0.003	3.272 ± 0.198	2.643 ± 0.218	2.416 ± 0.272	1.64 ± 0.15	0.00
−2.5	20.6 ± 8.7	133.4 ± 8.5	0.211 ± 0.004	3.485 ± 0.159	2.725 ± 0.177	2.481 ± 0.219	1.79 ± 0.12	0.00
−0.8	28.2 ± 8.3	135.1 ± 8.0	0.195 ± 0.004	3.033 ± 0.143	2.841 ± 0.159	3.077 ± 0.196	1.94 ± 0.11	0.02
0.1	20.0 ± 16.1	131.7 ± 9.7	0.196 ± 0.004	3.193 ± 0.132	2.686 ± 0.147	2.700 ± 0.181	2.26 ± 0.10	0.03
1.2	−1.5 ± 16.0	131.6 ± 12.2	0.205 ± 0.004	3.239 ± 0.148	2.625 ± 0.165	2.576 ± 0.197	1.89 ± 0.12	0.01
3.0	−28.9 ± 17.1	135.8 ± 10.9	0.204 ± 0.004	3.391 ± 0.159	2.723 ± 0.177	2.516 ± 0.220	1.45 ± 0.13	0.01
6.3	−53.3 ± 26.2	127.3 ± 10.7	0.205 ± 0.004	3.170 ± 0.197	2.397 ± 0.213	2.384 ± 0.270	1.80 ± 0.15	0.01
12.2	−76.7 ± 23.4	114.1 ± 9.0	0.183 ± 0.002	2.918 ± 0.197	2.444 ± 0.217	1.937 ± 0.269	1.79 ± 0.15	0.35
16.9	−100.8 ± 42.3	116.3 ± 28.2	0.175 ± 0.011	2.947 ± 0.444	2.116 ± 0.497	1.504 ± 0.590	−1.37 ± 0.38	3.84
NGC 7557								
−6.5	−24.9 ± 47.0	98.1 ± 32.1	0.176 ± 0.012	2.791 ± 0.473	2.701 ± 0.556	2.335 ± 0.673	1.81 ± 0.41	0.00
−2.2	−5.0 ± 20.6	104.9 ± 19.4	0.177 ± 0.004	3.106 ± 0.162	2.172 ± 0.192	2.010 ± 0.232	2.35 ± 0.14	0.00
−0.4	11.8 ± 20.7	103.6 ± 15.0	0.179 ± 0.004	2.954 ± 0.157	2.675 ± 0.187	2.349 ± 0.226	2.73 ± 0.13	0.00
0.3	19.1 ± 17.1	105.6 ± 15.0	0.172 ± 0.004	2.863 ± 0.157	2.830 ± 0.187	2.458 ± 0.226	2.88 ± 0.13	0.00
1.7	4.3 ± 26.1	104.0 ± 19.8	0.176 ± 0.004	3.239 ± 0.163	2.433 ± 0.193	2.395 ± 0.232	2.29 ± 0.14	0.00
5.7	−5.3 ± 55.5	118.4 ± 37.5	0.161 ± 0.013	2.724 ± 0.539	2.364 ± 0.633	1.820 ± 0.777	2.29 ± 0.46	0.00

Table B1 – *continued*

(1)	(2)	(3)	(4)	(5)	(6)	(7)	(8)	(9)
NGC 7631								
-9.226	-143.3 ± 47.2	113.1 ± 24.6	0.163 ± 0.010	2.509 ± 0.334	2.596 ± 0.389	1.902 ± 0.461	1.06 ± 0.28	0.37
-5.616	-53.1 ± 20.7	139.5 ± 14.8	0.180 ± 0.009	3.522 ± 0.304	2.792 ± 0.356	2.373 ± 0.442	1.67 ± 0.25	0.31
-2.481	-32.1 ± 23.0	138.6 ± 15.0	0.175 ± 0.008	3.177 ± 0.286	2.539 ± 0.337	2.124 ± 0.417	2.12 ± 0.24	0.14
-0.837	-24.2 ± 23.0	167.7 ± 15.0	0.164 ± 0.008	2.868 ± 0.286	2.820 ± 0.337	2.363 ± 0.417	0.48 ± 0.24	1.48
1.959	57.0 ± 23.3	142.4 ± 16.7	0.176 ± 0.008	3.561 ± 0.269	2.291 ± 0.318	2.294 ± 0.393	0.78 ± 0.23	1.11
5.142	74.6 ± 22.2	159.1 ± 12.8	0.186 ± 0.010	2.929 ± 0.336	3.139 ± 0.394	2.547 ± 0.481	1.34 ± 0.28	0.25
8.875	121.2 ± 37.1	155.7 ± 29.7	0.190 ± 0.020	3.672 ± 0.692	3.832 ± 0.822	2.705 ± 1.046	1.88 ± 0.60	0.28
NGC 7643								
-14.3	-129.4 ± 63.1	130.1 ± 65.6	0.165 ± 0.019	2.902 ± 0.792	3.195 ± 0.938	3.822 ± 1.093	-0.71 ± 0.71	2.74
-9.0	-86.5 ± 47.0	101.6 ± 34.4	0.175 ± 0.008	2.953 ± 0.315	2.810 ± 0.375	2.243 ± 0.452	1.40 ± 0.27	1.29
-2.9	-27.0 ± 37.4	116.5 ± 16.9	0.183 ± 0.006	3.334 ± 0.233	2.200 ± 0.273	2.157 ± 0.328	1.56 ± 0.20	1.09
-0.7	-4.7 ± 28.0	111.3 ± 13.0	0.145 ± 0.005	2.759 ± 0.195	2.201 ± 0.231	2.150 ± 0.278	0.21 ± 0.17	3.02
0.2	17.0 ± 28.0	116.9 ± 13.0	0.141 ± 0.005	2.711 ± 0.195	2.294 ± 0.231	2.062 ± 0.278	0.21 ± 0.17	2.67
1.4	25.6 ± 23.2	117.1 ± 10.0	0.168 ± 0.004	2.931 ± 0.158	2.262 ± 0.190	2.135 ± 0.229	0.86 ± 0.13	1.75
5.1	56.8 ± 44.4	121.6 ± 24.7	0.182 ± 0.008	3.096 ± 0.311	2.516 ± 0.374	2.195 ± 0.459	1.13 ± 0.27	1.39
11.6	148.2 ± 56.2	130.9 ± 66.5	0.161 ± 0.020	2.728 ± 0.803	2.465 ± 0.972	2.206 ± 1.196	1.51 ± 0.70	1.07

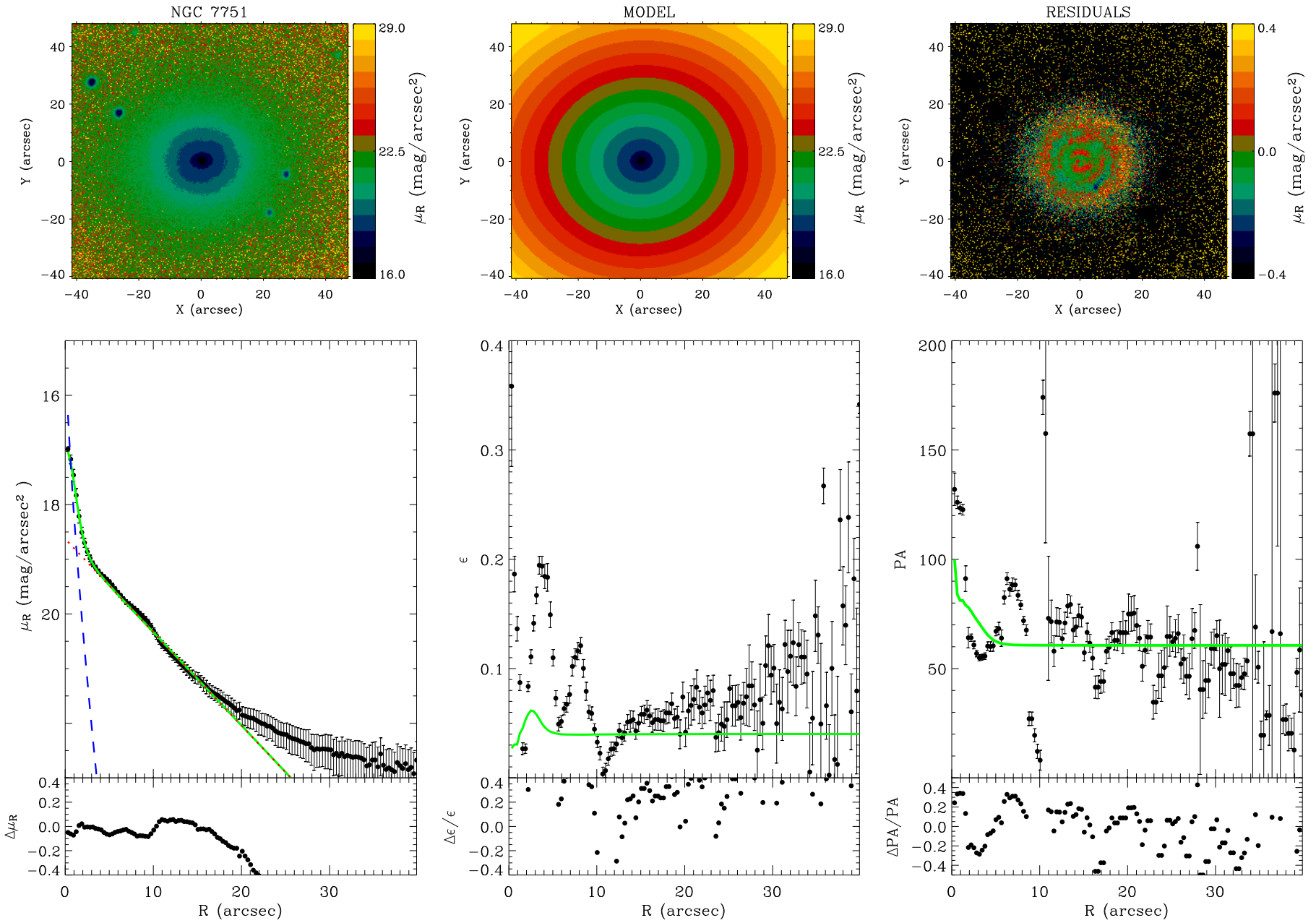
NGC 7751
MODEL
RESIDUALS
Y (arcsec)
X (arcsec)
μ_R (mag/arcsec^2)
29.0
22.5
16.0
0.4
0.0
−0.4
μ_R (mag/arcsec^2)
$\Delta\mu_R$
R (arcsec)
ϵ
$\Delta\epsilon/\epsilon$
PA
ΔPA/PA